The Astrophysical Journal, 676:163–183, 2008 March 20

THE SUBARU/*XMM-NEWTON* DEEP SURVEY (SXDS). V. OPTICALLY FAINT VARIABLE OBJECT SURVEY[1]

Tomoki Morokuma,[2,3] Mamoru Doi,[3] Naoki Yasuda,[4] Masayuki Akiyama,[5] Kazuhiro Sekiguchi,[2,5] Hisanori Furusawa,[5] Yoshihiro Ueda,[6] Tomonori Totani,[6] Takeshi Oda,[6,7] Tohru Nagao,[2,7] Nobunari Kashikawa,[2] Takashi Murayama,[8] Masami Ouchi,[9,10] Mike G. Watson,[11] Michael W. Richmond,[12] Christopher Lidman,[13] Saul Perlmutter,[14] Anthony L. Spadafora,[14] Greg Aldering,[14] Lifan Wang,[14,15] Isobel M. Hook,[16] and Rob A. Knop[17]

Received 2007 September 28; accepted 2007 November 30

ABSTRACT

We present our survey for optically faint variable objects using multiepoch (8–10 epochs over 2–4 years) i'-band imaging data obtained with Subaru Suprime-Cam over 0.918 deg^2 in the Subaru/*XMM-Newton* Deep Field (SXDF). We found 1040 optically variable objects by image subtraction for all the combinations of images at different epochs. This is the first statistical sample of variable objects at depths achieved with 8–10 m class telescopes or the *Hubble Space Telescope*. The detection limit for variable components is $i'_{\rm vari} \sim 25.5$ mag. These variable objects were classified into variable stars, supernovae (SNe), and active galactic nuclei (AGNs), based on the optical morphologies, magnitudes, colors, and optical–mid-infrared colors of the host objects, spatial offsets of variable components from the host objects, and light curves. Detection completeness was examined by simulating light curves for periodic and irregular variability. We detected optical variability for 36% ± 2% (51% ± 3% for a bright sample with $i' < 24.4$ mag) of X-ray sources in the field. Number densities of variable objects as functions of time intervals Δt and variable component magnitudes $i'_{\rm vari}$ are obtained. Number densities of variable stars, SNe, and AGNs are 120, 489, and 579 objects deg^{-2}, respectively. Bimodal distributions of variable stars in the color-magnitude diagrams indicate that the variable star sample consists of bright ($V \sim 22$ mag) blue variable stars of the halo population and faint ($V \sim 23.5$ mag) red variable stars of the disk population. There are a few candidates of RR Lyrae providing a possible number density of $\sim 10^{-2}$ kpc^{-3} at a distance of >150 kpc from the Galactic center.

Subject headings: galaxies: active — stars: variables: other — supernovae: general — surveys

1. INTRODUCTION

It is well known that there are a wide variety of objects showing optical variability by various mechanisms over various timescales in the universe. For example, stars in the instability strip in a color-magnitude diagram show periodic variability by pulsations (Cepheids and RR Lyrae), while cataclysmic variables show emergent variability induced by accretion flows from companion stars (novae), or magnetic reconnection or rotations (dwarf stars). Thermonuclear or core-collapse runaway explosions of massive stars are observed as supernovae (SNe). Recent studies of optical afterglows of gamma-ray bursts (GRBs), which are extremely energetic phenomena, are starting to reveal their nature. Active galactic nuclei (AGNs) show irregular flux variability not only in the optical but also at other wavelengths. The optically variable objects described above change their intrinsic brightness, but observed variability can have other causes. Searches for microlensing events have aimed to test the hypothesis that a significant fraction of the dark matter in the halo of our Galaxy could be made up of massive compact halo objects (MACHOs), such as brown dwarfs or planets. Many asteroids in the solar system have been found as moving objects. Many surveys for these optically variable objects have been carried out and have contributed to many important astronomical topics.

The cosmic distance ladder, for example, was established partly based on studies of optically variable objects that are standardizable

[1] Based in part on data collected at Subaru Telescope, which is operated by the National Astronomical Observatory of Japan. Based on observations (program GN-2002B-Q-30) obtained at the Gemini Observatory, which is operated by the Association of Universities for Research in Astronomy, Inc., under a cooperative agreement with the NSF on behalf of the Gemini partnership: the National Science Foundation (US), the Particle Physics and Astronomy Research Council (UK), the National Research Council (Canada), CONICYT (Chile), the Australian Research Council (Australia), CNPq (Brazil), and CONICET (Argentina).

[2] Optical and Infrared Astronomy Division, National Astronomical Observatory, 2-21-1 Osawa, Mitaka, Tokyo 181-8588, Japan.

[3] Institute of Astronomy, Graduate School of Science, University of Tokyo, 2-21-1, Osawa, Mitaka, Tokyo 181-0015, Japan.

[4] Institute for Cosmic Ray Research, University of Tokyo, Kashiwa, Chiba 277-8582, Japan.

[5] Subaru Telescope, National Astronomical Observatory of Japan, 650 North A'ohoku Place, Hilo, HI 96720.

[6] Department of Astronomy, Kyoto University, Sakyo-ku, Kyoto 606-8502, Japan.

[7] JSPS Fellow.

[8] Astronomical Institute, Graduate School of Science, Tohoku University, Aoba, Sendai 980-8578, Japan.

[9] Space Telescope Science Institute, 3700 San Martin Drive, Baltimore, MD 21218.

[10] Hubble Fellow.

[11] Department of Physics and Astronomy, University of Leicester, Leicester LE1 7RH, UK.

[12] Physics Department, Rochester Institute of Technology, Rochester, NY 14623.

[13] European Southern Observatory, Alonso de Cordova 3107, Vitacura, Casilla 19001, Santiago 19, Chile.

[14] Lawrence Berkeley National Laboratory, 1 Cyclotron Road, Berkeley, CA 94720.

[15] Physics Department, Texas A&M University, College Station, TX 77843.

[16] University of Oxford Astrophysics, Denys Wilkinson Building, Keble Road, Oxford OX1 3RH, UK.

[17] Department of Physics and Astronomy, Vanderbilt University, P.O. Box 1807, Nashville, TN 37240.

candles. Observations of variable stars in nearby galaxies enable us to determine distances to them via the period-luminosity relation of Cepheids (Sandage & Tammann 2006 and references therein). Recent deep high-resolution monitoring observations with *Hubble Space Telescope* (*HST*) increased the number of nearby galaxies whose distances were measured using Cepheids. Well-sampled light curves of Type Ia supernovae (SNe Ia) in galaxies with distance measurements from Cepheids (Saha et al. 2006) showed an empirical relation between their light curve shapes and their luminosities: intrinsically brighter SNe Ia declined more slowly in brightness (Phillips 1993). These relations have led to the discovery of an accelerated expansion of the universe by two independent SN Ia search teams (Perlmutter et al. 1998; Riess et al. 1998). In ongoing and planned SN surveys, SNe Ia are expected to set tight constraints on the value of the dark energy and its cosmological evolution, if any.

Variable stars have been also used to trace Galactic structure as standard candles. RR Lyrae stars are old (>8 Gyr), bright ($M_V \sim 0.6$ mag), low-mass pulsating stars with blue colors of $B - V \sim 0.3$, and are appropriate for tracing structures in the halo. They can be selected as stars showing large variability (0.5–1.0 mag in the V band) on short periods of 0.3–0.5 days (Vivas et al. 2004). RR Lyrae selected using multiepoch imaging data obtained by the Sloan Digital Sky Survey (SDSS; York et al. 2000) provided a possible cutoff of the Galactic halo at ~65 kpc from the Galactic center (Ivezić et al. 2000). The subsequent studies on RR Lyrae by SDSS (Ivezić et al. 2004a, 2005; Sesar et al. 2007) and the Quasar Equatorial Survey Team (QUEST; Vivas et al. 2004; Vivas & Zinn 2006) found many substructures in the Galactic halo, including those already known.

Optical variability of the first luminous AGN (quasar), 3C 273, was recognized (Smith & Hoffleit 1963) just after its discovery (Schmidt 1963). Since then, it has been found that almost all quasars show optical variability; indeed, it is one of common characteristics of AGNs. Quasar surveys such as SDSS and the Two Degree Field Quasar Redshift Survey (2QZ; Boyle et al. 2000) have been carried out mainly using optical multicolor selections. These surveys have made large catalogs of quasars (Croom et al. 2004; Schneider et al. 2005) and have also found very high-z quasars close to the reionization epoch (Fan et al. 2006a, 2006b). However, their efficiency in finding lower luminosity AGNs using color selections are expected to be low, because AGN components are faint compared with their host galaxy components. On the other hand, recent deep X-ray observations with the *ASCA*, *XMM-Newton*, and *Chandra* satellites have effectively found many distant low-luminosity AGNs, as well as obscured AGNs. Their better efficiency is due to the faintness of host galaxies in X-rays and the high transparency of dust to X-ray photons. X-ray observations can identify faint AGNs easily, while finding even unobscured AGNs is difficult using optical color selections.

However, since deep X-ray surveys over wide fields require a lot of telescope time (e.g., a 2 Ms exposure in the Chandra Deep Field–North; Brandt et al. 2001), optical variability is being recognized again as a good tracer for AGNs. Some studies have succeeded in detecting optical variability of quasars (Hook et al. 1994; Giveon et al. 1999; Hawkins 2002), and in finding many quasars by optical variability with a completeness as high as classical UV-excess selections (Hawkins & Veron 1993; Ivezić et al. 2003). Comparison of SDSS imaging data with older plate imaging data (de Vries et al. 2003, 2005; Sesar et al. 2006) and SDSS spectrophotometric data (Vanden Berk et al. 2004) shows a clear anticorrelation between quasar luminosity and optical variability amplitude, as indicated in previous studies (Hook et al. 1994; Giveon et al. 1999). Therefore, optical variability can be an efficient tool for finding low-luminosity AGNs if variable components can be extracted. Ultradeep optical variability surveys with Wide-Field Planetary Camera 2 (WFPC2) installed on *HST* actually found 24 galaxies with variable nuclei down to $V_{\rm nuc} = 27.5$ mag and $I_{\rm nuc} = 27$ mag, which are as faint as nearby Seyfert galaxies ($-15 < M_B < -19$) at $z \sim 1$ (Sarajedini et al. 2000, 2003). Cohen et al. (2006) also found several tens of AGNs by optical variability using multiepoch data with the Advanced Camera for Survey (ACS) on board *HST*. The number densities of AGNs selected via optical variability can be of the same order as those selected via deep X-ray observations (Brandt & Hasinger 2005). However, samples from the *HST* imaging data were not large enough for statistical studies. The comparable number densities of variability-selected AGNs may indicate that there could be several populations of AGNs with different properties. Furthermore, a search for faint transient objects with Suprime-Cam (Miyazaki et al. 2002) on the Subaru telescope revealed very faint AGN variability in the nuclei of apparently normal galaxies, and found that such nuclei show very rapid (~a few days) nuclear variability with a large fractional amplitude (Totani et al. 2005). Such behavior is similar to that of the Galactic center black hole, Sgr A*, rather than bright AGNs, possibly indicating a different physical nature for accretion disks of very low luminosity AGNs and very luminous AGNs.

Object variability could affect searches for rare objects using nonsimultaneous observational data. Iye et al. (2006) and Ota et al. (2007) searched for Lyα emitters (LAEs) at $z \sim 7.0$ by comparing narrowband data with broadband data obtained more than a few years earlier. They succeeded in identifying a bright candidate spectroscopically as a LAE at $z = 6.94$. Another candidate without spectroscopic identifications could be just a transient object, and the authors treated it as a marginal candidate. SN rate studies based on optical variability (Pain et al. 2002; Dahlen et al. 2004; Barris & Tonry 2006; Sullivan et al. 2006; Poznanski et al. 2007; T. Oda et al. 2008, in preparation) have sometimes confronted problems in classifying events due to insufficient observational data, such as spectroscopic identifications, time samplings, and multiwavelength measurements. Given limited time on large telescopes, one cannot make spectroscopic observations of all variable candidates; thus, multiwavelength imaging data and light curves in year-scale baselines are very useful to separate SNe from other kinds of variable objects.

Recently, many optical variability surveys with dense time samplings have been conducted for various astronomical purposes. Dividing exposure time into multiple epochs in extremely deep surveys using large or space telescopes also enables us to explore faint optical variability. Projects conducted recently or ongoing include the Faint Sky Variability Survey (FSVS; Groot et al. 2003), Deep Lens Survey (DLS; Becker et al. 2004), Supernova Legacy Survey (SNLS; Astier et al. 2006), Great Observatory Origins Deep Survey (GOODS; Strolger et al. 2004), Groth-Westphal Survey Strip (GSS; Sarajedini et al. 2006), Hubble Deep Field–North (HDF-N; Sarajedini et al. 2000, 2003), Hubble Ultra Deep Field (HUDF; Cohen et al. 2006), Sloan Digital Sky Survey-II (SDSS-II), and the Supernova Survey (Sako et al. 2008). Densely sampled observations targeting GRB orphan afterglows have also been carried out (e.g., Rau et al. 2006). We focus here on our survey for optically faint variable objects since 2002 in the Subaru/*XMM-Newton* Deep Field (SXDF, Sekiguchi et al. 2004, and 2008, in preparation). The data have been taken by the Subaru/*XMM-Newton* Deep Survey (SXDS) project. Our study described in this paper provides the first statistical sample of optically faint variable objects and is unique among studies using 8–10 m class

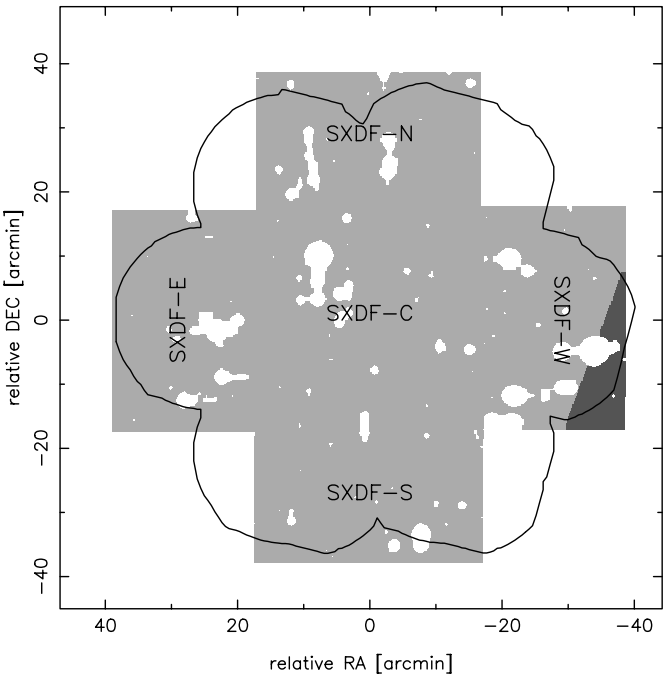

FIG. 1.— Suprime-Cam imaging fields (*light and dark gray regions*) in the SXDF, with superimposed *XMM-Newton* EPIC imaging fields (*black solid line*) and *Spitzer* IRAC imaging fields (*light gray region*). The coordinates are measured relative to the center of the SXDF, ($02^h18^m00^s$, $-05°00'00''$) in J2000.0. Our optically variable object survey has been carried out in the entire Suprime-Cam field over 0.918 deg^2, except for regions around bright objects (white blanks). The five pointings of the Suprime-Cam, SXDF-C, SXDF-N, SXDF-S, SXDF-E, and SXDF-W, are described.

telescopes and *HST* in its combination of wide-field coverage and depth. The Suprime-Cam imaging data and the analysis for finding optically variable objects are described in § 2, followed by other observational data in § 3. We describe object classifications in § 4 and detection completeness in § 5. The results are discussed for statistics of the whole sample in § 6 and for variable stars alone in § 7. We summarize our results in § 8. In this paper, we adopt throughout the AB magnitude system for optical and mid-infrared photometry.

2. OPTICALLY FAINT VARIABLE OBJECT SURVEY WITH SUBARU SUPRIME-CAM

2.1. *Subaru/XMM-Newton Deep Field* (*SXDF*)

We are carrying out an optically faint variable object survey using a wide-field camera, Suprime-Cam, on the prime focus of the Subaru 8.2 m telescope. The widest field of view ($34' \times 27'$) among the optical imaging instruments installed on *HST* and 8–10 m telescopes provides us a unique opportunity for statistical studies of rare and faint objects, which are less affected by cosmic variance than those derived from smaller fields.

The SXDF is centered on $02^h18^m00^s$, $-05°00'00''$ (J2000.0), in the direction toward the Galactic halo, (l, b) = (169°, −60°). The SXDF is an ongoing multiwavelength project from X-ray to radio (Sekiguchi et al. 2004, and 2008, in preparation), exploring aspects of the distant universe such as the nature of the extragalactic X-ray populations (Watson et al. 2005; Ueda et al. 2008; M. Akiyama et al. 2008, in preparation), large-scale structures at high redshift (Ouchi et al. 2005a, 2005b), and the cosmic history of mass assembly (Kodama et al. 2004; Yamada et al. 2005; Simpson et al. 2006). The field coverage is ∼1.2 deg^2, which consists of five pointings of Suprime-Cam (SXDF-C, SXDF-N, SXDF-S, SXDF-E, and SXDF-W, respectively; see Fig. 1). We use the i'-band-selected photometric catalogs in B, V, R_C, i', and z' bands, which are summarized in Furusawa et al. (2008). The depths of the catalogs that we use are almost the same among the five fields, 28.4, 27.8, 27.7, 27.7, and 26.6 mag (3 σ, 2.0″ diameter) in the B, V, R_C, i', and z' bands, respectively (Table 1). Optical photometric information used in this paper (except for variability measurements) is derived from these catalogs and are not corrected for the Galactic extinction in the SXDF direction, $E(B-V) = 0.019 - 0.023$ mag (Schlegel et al. 1998; see Furusawa et al. 2008).

2.2. *Subaru Suprime-Cam Imaging Data*

Our survey for optically faint variable objects in the SXDF is based on multiepoch i'-band Suprime-Cam imaging data, starting in September 2002 (Furusawa et al. 2008; N. Yasuda et al. 2008, in preparation). The Suprime-Cam observations are summarized in Table 2. These observations include those for an extensive high-z SN search using well-sampled i'-band images in 2002 (Yasuda et al. 2003, and 2008, in preparation), from which Doi et al. (2003) reported the discovery of 13 high-z SNe. In addition to observations used to make the catalogs in Furusawa et al. (2008), we carried out i'-band observations in 2005. The final images were taken in October 2003 in the two fields (SXDF-N and SXDF-W) and in September 2005 in the remaining three fields (SXDF-C, SXDF-N, and SXDF-E). The numbers of the observational epochs (N_{epoch}) in the five fields are 10, 8, 8, 10, and 8, respectively. Time intervals of the observations are from 1 day to 3 years in observed frame.

In each epoch, stacked images were made with a standard method for the Suprime-Cam data using the NEKO software (Yagi et al. 2002) and the SDFRED package (Ouchi et al. 2004). Some images taken on different dates were combined together to make

TABLE 1
IMAGING DATA OTHER THAN OPTICAL VARIABILITY

Wavelength	Telescope/Instrument	Band	Detection Limit	Area[a] (deg^2)	Variable[b]	Detection[c]
Optical.....	Subaru/Suprime-Cam[d]	B, V, R_C, i', z	28.2, 27.2, 27.6, 27.5, 26.5 mag[e]	0.918	1040	1040
X-ray	*XMM-Newton*/EPIC	2.0–10.0 keV	3×10^{-15} erg s^{-1} cm^{-2}	0.808	936	165
	XMM-Newton/EPIC	0.5–2.0 keV	1×10^{-15} erg s^{-1} cm^{-2}	0.808	936	91
Mid-infrared	*Spitzer*/IRAC	3.6 μm	22.0 mag[e]	0.889	1028	995

[a] Area overlapping with the variability survey field.
[b] Number of optically variable objects within the area.
[c] Number of optically variable objects detected in the bands within the area.
[d] Derived from preliminary version of the SXDF catalogs in Furusawa et al. (2008).
[e] Detection limits for optical and mid-infrared imaging are measured in AB magnitude.

TABLE 2
Summary of Subaru Suprime-Cam i'-band Imaging Observations for Variability Detections

Epoch	Date (UT)[a]	Δt[b]	t_{exp} (s)	θ[c] (arcsec)	m_{lim}[d]
		SXDF-C			
1.....	2002 Sep 29, 30	0.0	2700	0.54	26.19
2.....	2002 Nov 01	32.6	1860	0.92	25.76
3.....	2002 Nov 02	33.5	1800	0.68	25.85
4.....	2002 Nov 05	36.7	2400	0.70	26.11
5.....	2002 Nov 09	40.5	2460	0.60	25.77
6.....	2002 Nov 27, 29	59.8	4200	0.72	26.38
7.....	2002 Dec 07	68.4	3000	0.78	26.32
8.....	2003 Oct 20	385.7	5760	1.14	26.53
9.....	2003 Oct 21	386.5	7500	0.58	26.71
10.....	2005 Sep 28	1094.6	3600	1.00	26.04
		SXDF-N			
1.....	2002 Sep 29, 30	0.0	3300	0.56	26.26
2.....	2002 Nov 01	32.4	2640	0.96	25.88
3.....	2002 Nov 02	33.3	1800	0.68	25.86
4.....	2002 Nov 09	40.3	2100	0.64	25.78
5.....	2002 Nov 29	60.3	3300	0.74	26.27
6.....	2003 Sep 22	357.5	4264	0.60	26.37
7.....	2003 Oct 02	367.6	1500	0.70	25.88
8.....	2003 Oct 21	386.5	3000	0.72	26.14
		SXDF-S			
1.....	2002 Sep 29, 30	0.0	3000	0.52	26.28
2.....	2002 Nov 01	32.5	3600	1.04	25.91
3.....	2002 Nov 02	33.4	1800	0.70	25.83
4.....	2002 Nov 09	40.4	2580	0.66	25.60
5.....	2002 Nov 29	60.6	1500	0.82	26.00
6.....	2003 Sep 22	357.6	4500	0.54	26.45
7.....	2003 Oct 02	367.7	2040	0.68	26.00
8.....	2005 Sep 28	1094.6	3900	0.96	26.04
		SXDF-E			
1.....	2002 Sep 29, 30	0.0	3000	0.60	26.25
2.....	2002 Nov 01	32.5	3000	1.04	25.97
3.....	2002 Nov 02	33.4	1800	0.70	25.83
4.....	2002 Nov 09	40.4	2820	0.66	26.78
5.....	2002 Nov 29	60.6	1800	0.80	26.03
6.....	2002 Dec 07	68.6	1209	1.54	25.19
7.....	2003 Sep 22	357.6	6000	0.62	26.58
8.....	2003 Oct 02	367.7	1271	0.68	25.71
9.....	2003 Oct 21	386.7	1400	0.88	25.51
10.....	2005 Sep 28	1094.6	3600	0.96	26.11
		SXDF-W			
1.....	2002 Sep 29, 30	0.0	2400	0.54	26.14
2.....	2002 Nov 01	32.7	3000	0.96	25.96
3.....	2002 Nov 02	33.5	1800	0.66	25.84
4.....	2002 Nov 05	36.8	3060	0.76	25.98
5.....	2002 Nov 09	40.5	2100	0.64	25.97
6.....	2002 Nov 27, 29	59.8	4200	0.74	26.39
7.....	2002 Dec 07	68.5	6483	1.04	26.34
8.....	2003 Oct 20, 21	386.5	5460	0.66	26.46

[a] Observed date. When the images were stacked together with those at different dates, both dates are included.
[b] Days from the first observation in each field.
[c] FWHM of PSF in stacked images.
[d] Limiting magnitude of 5 σ in 2.0″ aperture.

all the depths almost the same. Then we geometrically transformed the images using the `geomap` and `geotran` tasks in IRAF[18] in order to match the coordinates more accurately to each other. The root-mean-square of residuals of the coordinate differences are typically 0.4 pixel.

Typical exposure times of 1 hr provide limiting magnitudes of $m_{lim} = 25.2–26.8$ mag ($\langle m_{lim}\rangle_{median} = 26.0$ mag, 5 σ, 2.0″ diameter). The full width at half-maximum (FWHM) values of the point spread function (PSF) were $\theta = 0.52''–1.54''$ ($\langle\theta\rangle_{median} = 0.70''$; see Table 2).[19]

For our variability study, we used regions overlapping in all the epochs in each field. Considering saturation and nonlinearity of CCDs at high signal levels, we excluded regions around bright objects to ensure reliable detection of object variability. The total effective area is 0.918 deg^2 (Table 1), shown as light and dark gray regions in Figure 1.

2.3. *Variability Detection*

The Suprime-Cam images have different PSF size (and shape) in every epoch because of time-varying atmospheric seeing. Therefore, we cannot measure variability of objects by simply comparing flux within a fixed small aperture, as Sarajedini et al. (2000, 2003) did for the *HST* WFPC2 images. Cohen et al. (2006) used total magnitude for variability detections in the images obtained with the Advanced Camera for Survey (ACS) on *HST*, because the PSF varied with locations on the CCDs of ACS. Accurate photometry itself of any kind for extended objects is often difficult. Since variable components are almost always point sources, the light from nonvariable extended components just increases the noise for variability detections. Hence, we used an image-subtraction method introduced by Alard & Lupton (1998) and developed by Alard (2000), instead of using total magnitudes of objects. This subtraction method using space-varying convolution kernels, which are obtained by fitting kernel solutions in small subareas, enables us to match one image against another image with a different PSF. We can then detect and measure variable objects in the subtracted images. We applied this method for all possible pairs[20] of stacked images at different epochs and detected variability of the objects in each field. Figure 2 shows examples of the image subtraction for three of the variable objects.

We now describe details of the procedures for variability detection and our definitions of variable objects. First, we smoothed all the subtracted images with the PSFs and detected positive and negative peaks of surface brightness in subpixel unit. Then, in all the subtracted images, we selected objects whose aperture flux in a fixed diameter of 2.0″ were above $5\sigma_{bf}$ or below $-5\sigma_{bf}$ of the background fluctuations (σ_{bf}) within the same aperture. The background fluctuation σ_{bf} is obtained by calculating the standard deviation of 2.0″ aperture flux in ~200 places around each positive or negative peak in the subtracted images. We inspected these variable candidates visually to exclude candidates around mis-subtracted regions. Second, we defined the central coordinates of the variable object candidates as the flux-weighted averages of all the coordinates where significant variability were detected in the subtracted images in the first procedure. Third, we did 2.0″ diameter aperture photometry for all these variable object candidates in the subtracted images, the reference images of which were an

[18] IRAF is distributed by the National Optical Astronomy Observatories, which are operated by the Association of Universities for Research in Astronomy, Inc., under cooperative agreement with the National Science Foundation.
[19] Pixel scale of Suprime-Cam is 0.202″ pixel^{-1}.
[20] The number of the combinations is ${}_{N_{epoch}}C_2$.

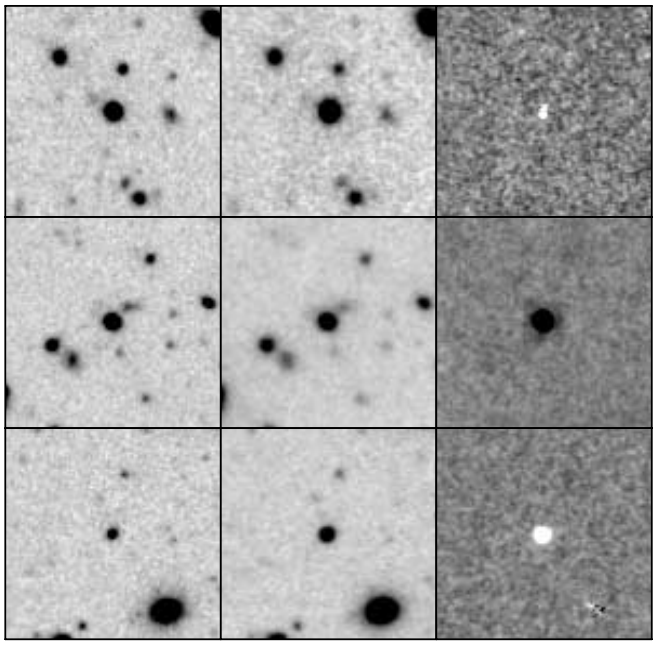

FIG. 2.—Examples of variability detection. In each row, an image on a reference date, an image on another date, and subtracted image are shown from left to right. Variable objects are clearly seen as positive or negative residuals in the right panels. All these three objects were spectroscopically identified. The top object is a M dwarf star, the middle object is a broad-line AGN at $z = 2.150$, and the bottom object is a SN Ia at $z = 0.606$. The spectra and light curves are shown in the top row of Fig. 3, the third row of Fig. 5, and the bottom row of Fig. 5, respectively. The box sizes are $20''$.

image with the smallest PSF size in each field,[21] and scaled the aperture measurements to the total flux, assuming that the variable components were always point sources. The factors used to scale the $2.0''$ aperture flux to total flux were calculated as the ratio between the $2.0''$ aperture flux and total flux for point sources in each image (typically $\sim$1.1–1.3). We constructed total flux light curves of all the candidates and defined optically variable objects as objects showing more than $5\sigma_{\rm lc}$ (where $\sigma_{\rm lc}$ is the photometric error in the light curves) variability in at least one combination of the epochs in the light curves. We note that some variable objects have unreliable photometric points in the light curves. In the subtraction method, very slight offsets (even $\sim$0.05 pixel) for bright objects between the two images used for the subtraction could provide significant *dipole* subtractions. When an object has both a positive peak above $5\sigma_{\rm bf}$ and a negative peak below $-5\sigma_{\rm bf}$ locally (around $\sim$10 pixel square) in a certain subtracted image used to make the light curve, the photometric point of the object at that epoch is regarded as unreliable. These epochs were not used in evaluating variability.

We followed these procedures for all the five fields. Finally, we made an optically variable object catalog consisting of 1184 objects in the area of 0.918 deg^2 (1290 variable objects deg^{-2}). However, for widely spread galaxies or bright objects, subtracted images are sometimes insecurely extended and show bumpy features, although saturated or nonlinearity pixels were removed from the detections in advance. Variability of these objects is considered marginal. When we exclude such marginally variable objects, the number of variable objects is 1040 (1133 variable objects deg^{-2}). These 1040 variable objects have 9236 photometric points in their light curves, and 359 unreliably measured photometric points (3.9%) of 169 objects were not used in evaluating variability. In the following discussions, we use this secure sample of 1040 variable objects. We note that detection completeness is discussed in § 5.

In principle, variability should be measured as changes of luminosity of objects. To do so, it is necessary to measure total flux of variable objects. However, this is possible only for point sources such as variable stars and quasars whose luminosity is much larger than that of their host galaxies. To measure variable AGNs separately from their host galaxies is difficult using ground-based imaging data, especially when the flux of variable object is faint compared to the flux of the host. We measure the flux of the variable component ($\Delta f \equiv f_1 - f_2$) as describe above. In this paper, we use variable component magnitudes ($i'_{\rm vari} \equiv -2.5\log(|\Delta f|) + m_{\rm zero}$) to describe object variability, and we adopt the total magnitudes which are measured in the SXDF catalogs as the magnitudes of host objects.

2.4. *Assignment of Host Objects*

In order to investigate how far the variable components are located from the centers of possible host objects, and their properties such as magnitudes and colors in the catalogs, we assigned host objects to all the variable objects. In general, AGNs and SNe have their host galaxies, while variable stars have no host objects. In this paper, we defined variable stars themselves as host objects in order to treat all the variable objects equally. We calculated projected distances of the variable components from the surrounding objects in the stacked images taken when the variable objects were in the faintest phases, and defined the nearest object as the host object. The positions of the host objects were measured as peaks of surface brightness of the images smoothed by the PSFs. In the faintest phases of variable objects which may disappear (i.e., SNe), host objects should be detected, but high-z SNe which occur in diffuse galaxies seem hostless in some cases. Assigned host objects for such SNe may not be real host galaxies. It is also possible that transient objects on faint host objects may have no equivalent host objects in the SXDF catalogs, because the SXDF i'-band images for the catalogs were made by stacking all the exposures except for those in 2005. Among 1040 variable objects, the number of such objects, which do not have equivalent objects in the SXDF catalogs, is 8. These possible transient objects may be hostless SNe and are treated as SNe if their light curves satisfy a criterion described in § 4.2.2. The number of possible transient objects is small, and we do not exclude or discriminate them in most of the following discussions. In § 6 we discuss number densities of transient objects, which are defined as objects not detected in their faint phases; objects appear in some epochs at positions where there are no objects detected in other epochs. In this paper, the number of detections for each transient object is not considered in the definition of transient objects.

Information on host objects, such as total magnitudes and colors, is derived from integrated images, which were obtained in various epochs in each band, as shown in Furusawa et al. (2008), and they are averaged over the observational time spans. Therefore, properties of objects are appropriate for statistical studies and could be inaccurate if we focus on a certain object.

3. ADDITIONAL OBSERVATIONAL DATA

The SXDF project has carried out multiwavelength observations from X-ray to radio and follow-up optical spectroscopy. In this paper, optical spectroscopic results and X-ray imaging data are used to confirm the validity of our object classifications. X-ray data are also used for evaluating the completeness of AGN variability detection. We use mid-infrared imaging data to classify

[21] They are images obtained on 2002 September 29 and 30 for all the fields.

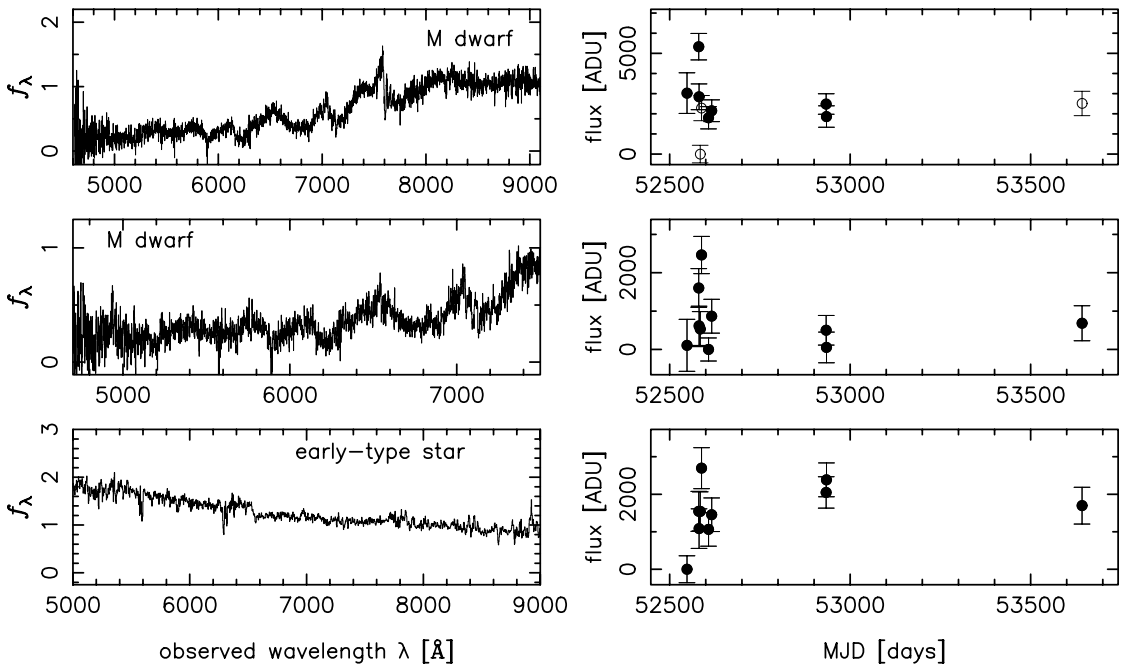

FIG. 3.—Spectra in arbitrary units and light curves of three variable stars. All the spectra were obtained with FOCAS on Subaru telescope. The observational configurations were the 300B grism and SY47 order-sort filter for the top two stars, and the 150 grism and SY47 order-sort filter for the bottom star. The top two rows are M dwarf stars with $B - V = 1.34$ and 1.36. The bottom row is an early-type star with $B - V = 0.44$. The light curves of differential flux were plotted in filled circles in linear scale (in ADU), because we cannot plot magnitudes in their faintest phases. The zero point is 34.02 mag. Unreliable photometric points are plotted with open circles.

optically variable objects in § 4. In this section, we summarize these observations and cross-identifications of optically variable objects. A summary of the X-ray and mid-infrared imaging data is given in Table 1.

3.1. *Optical Spectroscopy*

Since 2002, follow-up optical spectroscopic observations have been conducted with many telescopes and instruments (Yasuda et al. 2003, and in preparation; Yamada et al. 2005; Lidman et al. 2005; Watson et al. 2005; Ouchi et al. 2005a, 2005b). Instruments and telescopes used are the Two Degree Field (2dF) on the Anglo-Australian Telescope (AAT), the Faint Object Camera and Spectrograph (FOCAS; Kashikawa et al. 2002) on the Subaru telescope, the Visible Multiobject Spectrograph (VIMOS; Le Fevre et al. 2003) and the Focal Reducer/Low Dispersion Spectrograph 2 (FORS2) on the Very Large Telescope (VLT), the Gemini Multi-Object Spectrograph (GMOS; Hook et al. 2004) on the Gemini-North telescope, and the Echellette Spectrograph and Imager (ESI; Sheinis et al. 2002) on the Keck-II telescope. All the observations except for the Keck-II ESI, which is a high-dispersion echellete spectrograph, have been carried out in relatively low spectral resolution mode ($R \sim 500$). Most of the spectroscopic observations were done in multiobject spectroscopy mode.

Out of 1040 variable objects, 119 objects were targeted for spectroscopy. Of these 119 objects, 99 objects were identified and the redshifts were determined. The spectroscopic sample includes 3 stars, 14 host galaxies of SNe, 6 of which are spectroscopically identified as SNe Ia (Lidman et al. 2005; Yasuda et al. 2008, in preparation), 53 broad-line AGNs, 4 [Ne v] emitting galaxies, and 25 galaxies. Strong [Ne v] emission lines are only observed among AGNs, which emit strong ionizing photons above 97.2 eV, and [Ne v] emitting galaxies are considered to host AGNs. Other galaxies which appear to be normal galaxies also can host not only SNe but also AGNs, because many AGNs in our sample are faint compared to the host galaxies, so that the spectra may not show significant features of AGN origin. The redshifts of 96 extragalactic variable objects are $0.240 < z < 4.467$. We show 11 examples of the spectra obtained with FOCAS on Subaru and FORS2 on VLT in Figures 3, 4, and 5. The top two rows of Figure 3 are those for M dwarf stars showing bursts in 2002 with red optical colors of $B - V = 1.34$ and 1.36. The bottom row of Figure 3 is an early-type star with $B - V = 0.44$. We also show spectra of four broad-line AGNs at $z = 0.867$, 1.066, 2.150, and 3.553 in Figure 4, and spectra of SN host galaxies at $z = 1.239$, 0.505, 0.517, 0.606 in Figure 5. The light curves are also shown in the figures. The photometric points in these light curves are measured as differential flux in the subtracted images.

Since spectroscopic observations of variable objects were mainly targeted for X-ray sources and high-z SN candidates, the spectroscopic sample of variable objects are biased for those classes of variable objects. Therefore, we cannot say much about the fraction of variable objects from the spectroscopic sample alone.

3.2. *X-Ray Imaging*

X-ray imaging observations in the SXDF were carried out with the European Photon Imaging Camera (EPIC) on board *XMM-Newton*. They consist of one deep (∼100 ks) pointing on the center of the SXDF and six shallower (∼50 ks) pointings at the surrounding regions. In total, X-ray imaging covers most of the Suprime-Cam imaging fields (see Fig. 1). Details of the *XMM-Newton* EPIC observations, data analyses, and optical identifications are described in Ueda et al. (2008) and M. Akiyama et al. (2008, in preparation). The limiting fluxes are down to 1×10^{-15} erg^{-1} cm^{-2} s^{-1} in the soft band (0.5–2.0 keV) and 3×10^{-15} erg^{-1} cm^{-2} s^{-1} in the hard band (2.0–10.0 keV).

In this paper, we use a sample that was detected with likelihood >9 in either the soft or hard band and also within our variability survey fields. After excluding objects in the regions not used for variability detection (Table 1), we have 481 X-ray sources over

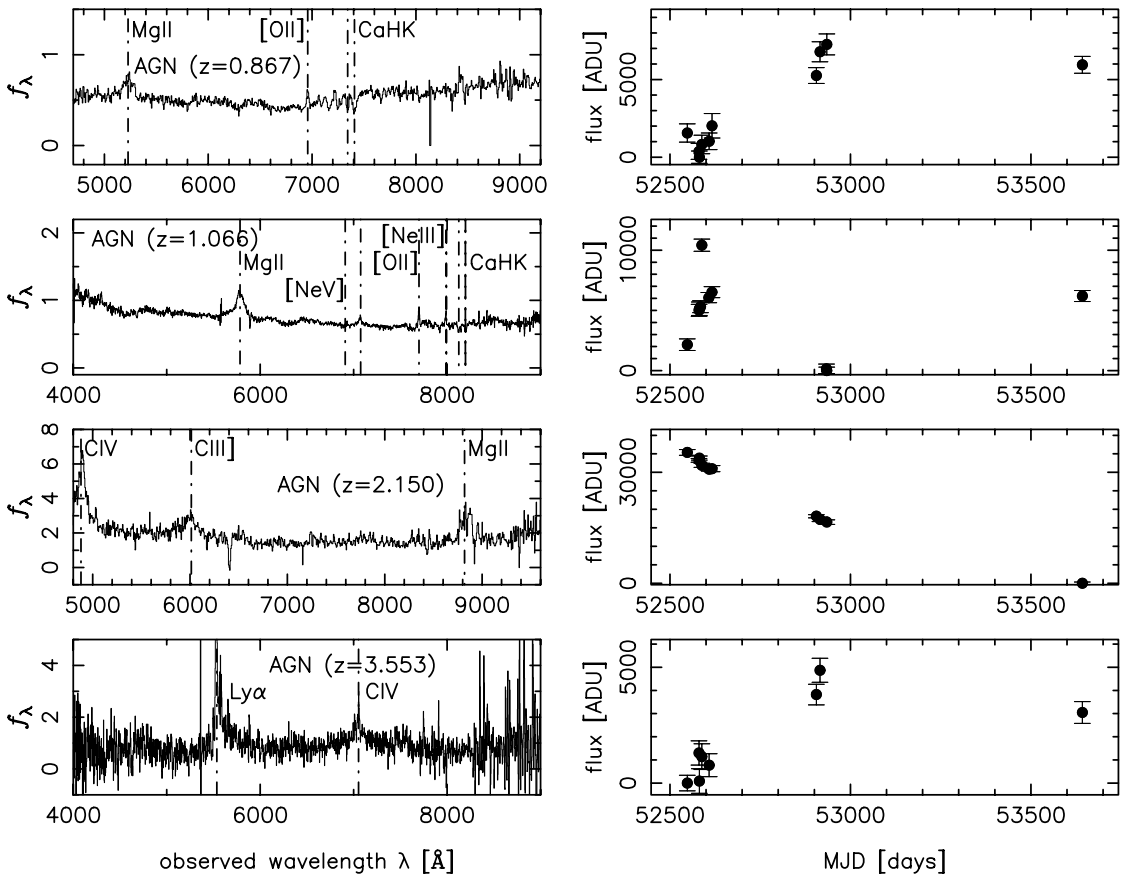

FIG. 4.—Spectra in arbitrary units and light curves of four extragalactic variable objects that are classified as AGNs based on their light curves and variable locations (central variability). All the spectra were obtained with FOCAS on Subaru telescope. The observational configurations were the 300B grism without any order-sort filters for the top and third AGNs, and the 150 grism and SY47 order-sort filter for the second and bottom AGNs. The redshifts are 0.867, 1.066, 2.150, and 3.553, from top to bottom. Dashed lines indicate detected emission and absorption lines. The zero point the light curves is 34.02 mag.

0.808 deg^2. Among 936 variable objects within the X-ray field, 172 objects were detected in X-rays (165 and 91 objects detected in the soft and hard bands, respectively; see Table 1).

3.3. *Mid-Infrared Imaging*

Mid-infrared imaging data in 3.6 μm, 4.5 μm, 5.8 μm, and 8.0 μm bands with the Infrared Array Camera (IRAC; Fazio et al. 2004) on *Spitzer* were obtained in the SXDF as a part of the *Spitzer* Wide-area Infrared Extragalactic (SWIRE; Lonsdale et al. 2003, 2004) survey. The IRAC data cover almost the entire Suprime-Cam field except for a part of SXDF-W. The covered field is 0.889 deg^2 (97% of the Suprime-Cam field), shown as gray regions in Figure 1. The reduced IRAC images were obtained from the SWIRE Archive, and the catalogs were made by M. Akiyama et al. (2008, in preparation). They use the IRAC imaging data for optical identifications of X-ray sources. In this paper, we use only the 3.6 μm band data for object classification in § 4. The limiting magnitude is ~22.0 mag (total flux, 5 σ for point sources). Among 1040 variable objects, 1028 objects are within the IRAC field, and 995 objects are detected in the 3.6 μm band (Table 1). Spatial resolution of the IRAC 3.6 μm band is not high, ~1″, but we can assign IRAC identifications to almost all the optically variable objects with good accuracy.

4. OBJECT CLASSIFICATION

The variable object sample includes several classes of variable objects. In this section, we classify these variable objects into variable stars, SNe, and AGNs using optical and mid-infrared imaging parameters. The procedures described in §§ 4.1 and § 4.2 are summarized in a flow chart of Figure 6.

We note again that the object photometric information is averaged over the observational time spans, but its effect on our statistical classifications and discussions is small even if objects are variable.

4.1. *Star Selection*

We extracted variable stars from the variable object sample using the Suprime-Cam optical imaging and the IRAC mid-infrared imaging data. Since the IRAC data cover 97% of the variability survey field in the SXDF, we concentrate on the 1028 variable objects in the overlapped region of 0.889 deg^2 for the following discussions, such as object classifications and number densities. Star selection is based on the optical morphologies, optical magnitudes, optical colors, and optical and mid-infrared colors of the variable objects. We used total magnitudes in both optical and mid-infrared wavelengths to make this selection.

4.1.1. *Criteria for Optical Morphology, Magnitude, and Color*

First, we assigned to all the variable objects *morphological scores* ($m_{\rm score} = 0$–10) and *color scores* ($c_{\rm score} = 0.00$–1.00) using a method described in Richmond (2005). The morphological scores $m_{\rm score}$ were calculated based on magnitude differences $\delta \equiv m_2 - m_3$ between 2.0″ aperture magnitudes (m_2) and 3.0″ aperture magnitudes (m_3), and the CLASS_STAR values in all the five broad-bands from the SExtractor (Bertin & Arnouts 1996) outputs in the SXDF catalogs. If an object has $0.10 < \delta < 0.20$, we add 1 to $m_{\rm score}$. If a CLASS_STAR value of an object is larger than some

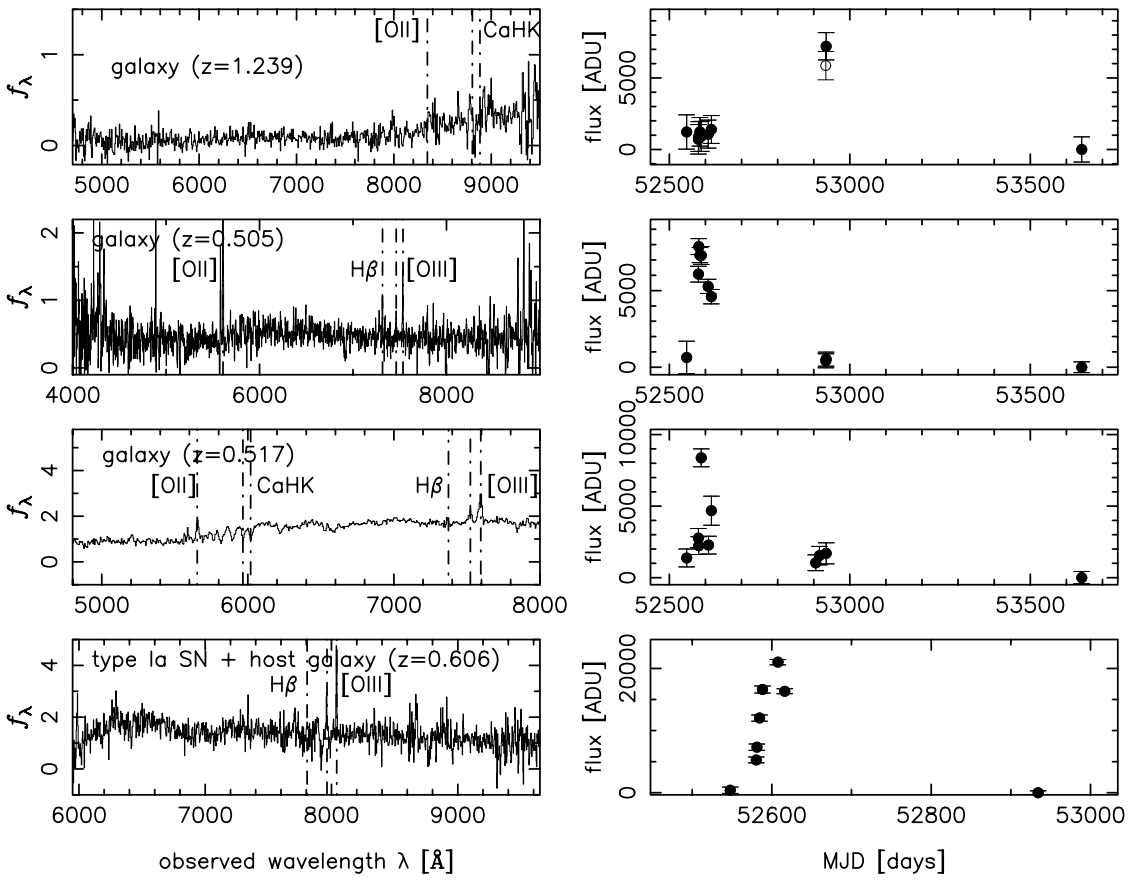

FIG. 5.—Spectra in arbitrary units and light curves of four extragalactic variable objects. The top three objects are classified as SNe based on their light curves and variable locations (offset variability). The bottom object was spectroscopically identified as a SN Ia, SN 2002km (Lidman et al. 2005), but we cannot determine whether they are SNe or AGNs because baselines of their light curves are not long enough (see § 4.2.2). The top three objects were observed with FOCAS on Subaru telescope. The observational configurations were the 150 grism without any order-sort filters for the top and third objects, and the 300B grism and SY47 order-sort filter for the second object. The bottom object were observed with FORS2 on VLT using the 300I grism and the OG590 order-sort filter (see Fig. A.32 in Lidman et al. 2005 for the SN component). The redshifts are 1.239, 0.505, 0.517, and 0.606, from top to bottom. Dashed lines indicate detected emission and absorption lines. The zero point is 34.02 mag.

value (typically 0.90, small variations from field to field) we also add 1 to $m_{\rm score}$. The color scores $c_{\rm score}$ were assigned based on the distances from the stellar loci in two color-color planes, $B-V$ versus $V-R$ and $V-R$ versus $R-i'$, using the SExtractor output IsophotMag. The stellar loci were defined using colors of a small set of bright stars. The color score represents the probability that each object is inside the stellar locus in color-color space using a Monte Carlo approach. A measure of the degree to which the colors of an object (including their uncertainties) fall within the stellar locus at the point of closest approach. Values range from 0.0 (color is completely outside the stellar locus) to 1.0 (color is completely within the locus). Objects with larger values for both scores are more likely to be stars, and the most likely stars should have $m_{\rm score} \geq 9$ and $c_{\rm score} \geq 0.90$. However, faint, red or blue stars are likely to have lower values for both the scores because of the low signal-to-noise ratio of photometry in some bands. In this classification, stars redder than G stars were not used for determining the stellar loci. The reddest stellar locus is at $R-i' \sim 1.7$. Therefore, red stars with $R-i' > 1.7$ cannot have high values of $c_{\rm score}$, and we do not use $c_{\rm score}$ values for red stars with $R-i' > 1.7$. Galaxies with similar colors can contaminate the sample. However, they can be excluded by an optical–mid-infrared color selection described below. Another problem is color differences of stars due to differences in their metallicity. Bright stars used for determining the stellar loci are mainly disk stars, while fainter stars are likely to belong to the halo population. Color differences in $R-i'$ caused by the population difference appear at $R-i' > 1.0$, so faint red stars with $R-i' > 1.0$ tend to have low $c_{\rm score}$ values; we decided to classify pointlike objects with $R-i' > 1.0$ as stars. Hence, we first assigned stellar likelihood to all the variable objects through five criteria using only optical photometric information:

(a) Stars with $m_{\rm score} \geq 9$ and $c_{\rm score} \geq 0.90$ (pointlike objects with stellar colors).

(b1) Probable stars with $9 > m_{\rm score} \geq 6$ and $0.90 > c_{\rm score} \geq 0.60$ (less pointlike objects with less stellar colors).

(b2) Probable stars with $m_{\rm score} \geq 9$ and $R-i' > 1.0$ (pointlike objects with red colors).

(c) Possible stars with $R-i' > 1.7$ (objects with very red colors).

(d) Nonstellar objects, which do not satisfy any criteria above.

Objects satisfying one of the criteria a, b1, b2, or c, are considered as stars.

In order to check the validity of our star selections based on only optical imaging parameters, we used a population synthesis model (Besançon model; Robin et al. 2003). We investigated the expected distributions of stars, including nonvariable stars in the SXDF which were selected with the same criteria in a $B-V$ versus V color-magnitude diagram. The distributions contain three sequences, and two of them, sequences for younger disk population and older halo population, are reasonably duplicated by the model. Another sequence of faint blue pointlike objects has almost the same distribution as more extended galaxies in this diagram. Then, we concluded that these faint blue pointlike objects are

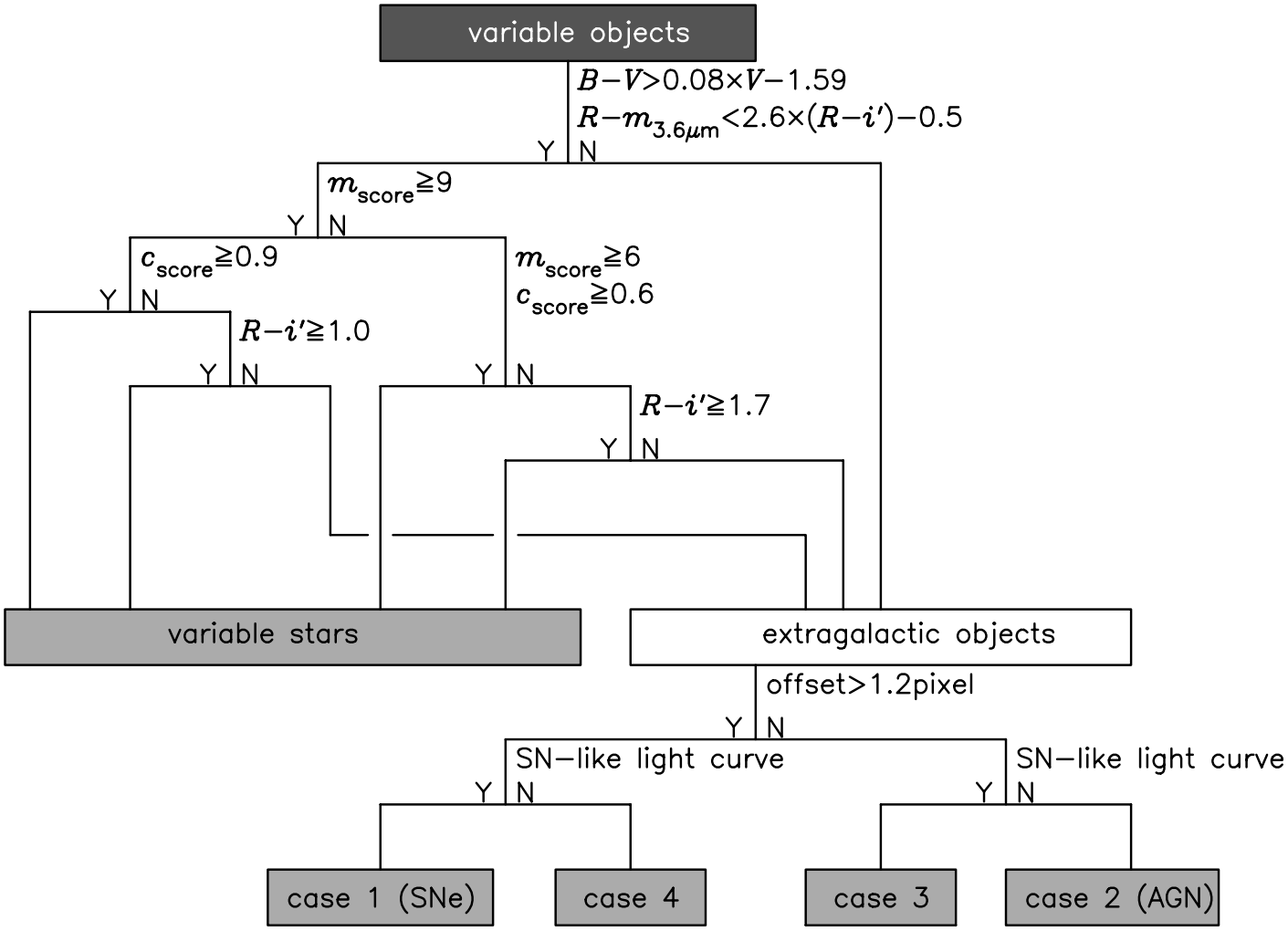

FIG. 6.— Flow chart of object classification. See the text in §§ 4.1 and 4.2 for details. If an object satisfies a criterion at some point along the path, it goes to the left; if not, to the right. In the first criteria, the IRAC data is necessary, so that we can classify variable objects in 97% of the overall field. The last criteria, using light curves for extragalactic objects, requires time baselines over longer than three years, and therefore only objects in the three fields, SXDF-C, SXDF-S, and SXDF-E, can be classified.

galaxies, and adopted one more criterion, $B - V > 0.08V - 1.59$ (dashed line in the top panel of Fig. 7), to exclude them.

4.1.2. *Criteria for Optical–Mid-Infrared Color*

Second, we investigated optical–mid-infrared colors of the variable objects in a $R - i'$ versus $R - m_{3.6\mu m}$ color-color plane. As shown in previous studies on object distributions in optical and mid-infrared color-color planes (Eisenhardt et al. 2004; Rowan-Robinson et al. 2005), stars and galaxies are more distinctly separated in optical–mid-infrared color-color planes than in purely optical color-color planes, because of the very different temperatures of stars and dust. Figure 7 shows color-color diagrams of the variable objects for $R - i'$ versus $i' - z'$ in the bottom left panel and $R - i'$ versus $R - m_{3.6\mu m}$ in the bottom right panel. A galaxy sequence extends widely from bottom to top on the blue side of $R - i'$ colors in the $R - i'$ versus $R - m_{3.6\mu m}$ color-color plane, while the stellar sequence shows a sharp distribution below the line in the figure. We defined variable objects satisfying a color criterion $R - m_{3.6\mu m} < 2.6(R - i') - 0.5$ as stars.

4.1.3. *Results of Star Selection*

Finally, we combined two independent criteria for stars and classified the variable objects into four categories;

1. *Reliable stars*: Variable objects that are selected as stars by criterion (a) and have stellar optical–mid-infrared colors (78).

2. *Probable stars*: Variable objects that are selected as probable stars by criterion (b1) or (b2) and have stellar optical-mid-infrared colors (24).

3. *Possible stars*: Variable objects that are selected as possible stars by criterion (c) and have stellar optical–mid-infrared colors (5).

4. *Nonstellar Objects*: Variable objects that do not have stellar optical–mid-infrared colors or are categorized as nonstellar objects by criterion (d) (921).

All the objects in categories 1, 2, and 3 satisfy the optical color-magnitude criterion ($B - V > 0.08V - 1.59$). The number of selected variable objects in each category is given at then end in parentheses. In Figure 7, filled circles show reliable stars (category 1), and open circles show probable stars (category 2) and possible stars (category 3).

We have three spectroscopically identified variable stars: an early-type star and two M dwarf stars. All these stars are securely classified as stars. The early-type star and one M dwarf star are classified as reliable stars. Another M dwarf star is classified as a probable star, with a red color of $R - i' = 1.14$, a high morphological score of $m_{score} = 9$ (i.e., a point source), and a low color score of $c_{score} = 0.34$.

The stellar and galaxy sequences in the $R - i'$ versus $R - m_{3.6\mu m}$ color-color diagram join together around $R - i' \sim 0.2$ and $R - m_{3.6\mu m} \sim 0$. Objects in this region can be contaminated with

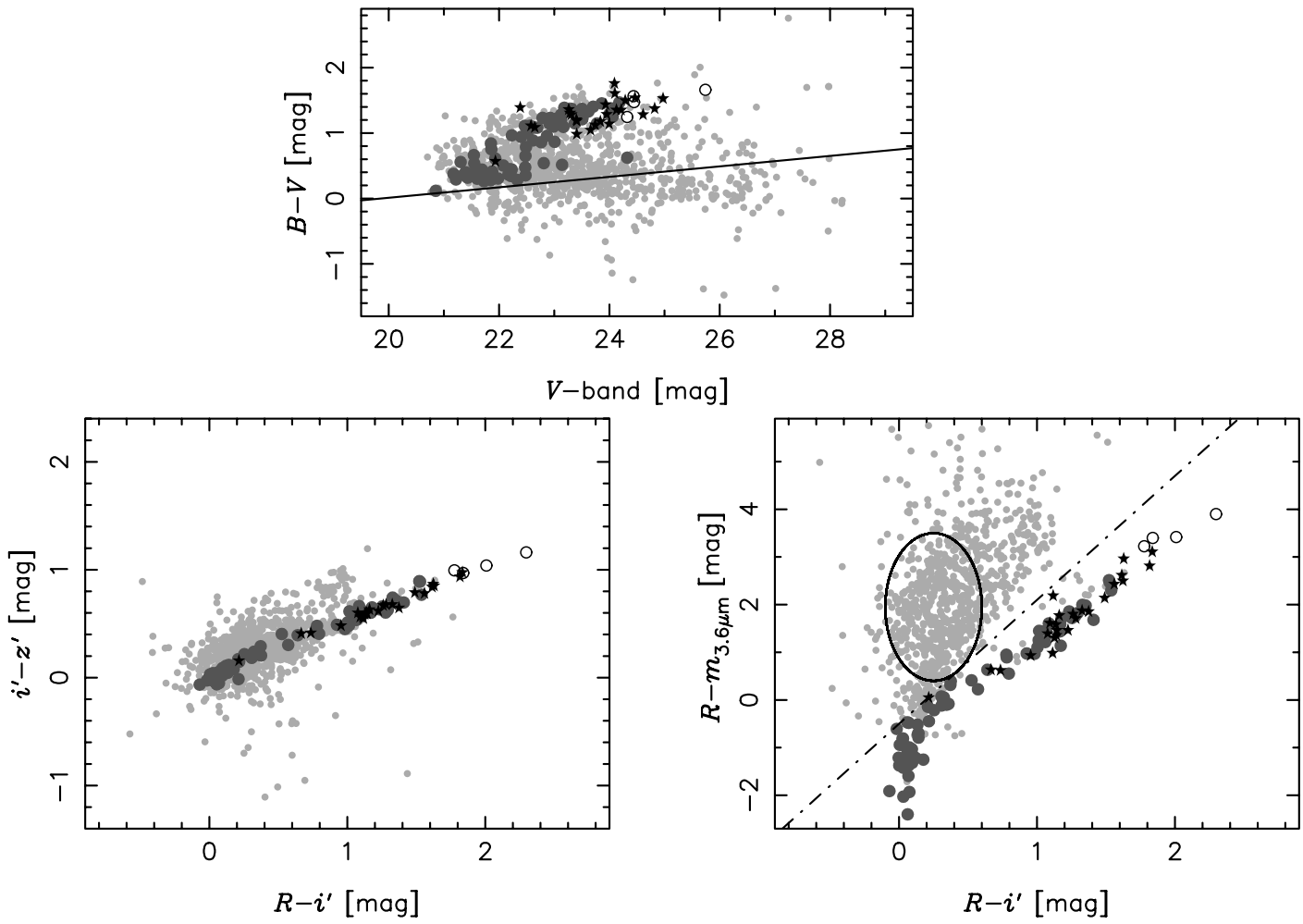

FIG. 7.—Color-color diagrams of variable objects in $R - i'$ vs. $i' - z'$ (*bottom left*) and $R - i'$ vs. $R - m_{3.6\mu m}$ (*bottom right*). We plot all the variable objects as small gray triangles, probable stars as large open circles, and reliable stars as large filled circles. A criterion indicated by the dashed line in the top panel, $B - V > 0.08V - 1.59$, is adopted to exclude pointlike blue galaxies. The dot-dashed line in the bottom right panel is a line separating stars and galaxies, $R - m_{3.6\mu m} = 2.6(R - i') - 0.5$. A large ellipse indicates a region of SDSS quasar ($0.1 < z < 5.2$) colors, $r - i : r - m_{3.6\mu m}$, in Hatziminaoglou et al. (2005) and Richards et al. (2006).

galaxies. There are several spectroscopically identified galaxies in the region, although they are not recognized as stars due to their optical extended morphologies. Point sources showing optical variability can be luminous quasars, but optical–mid-infrared colors of quasars are red enough to be distinguished from stars. All the 35 SDSS quasars at $0.2 < z < 3.7$ (Hatziminaoglou et al. 2005) and 259 SDSS quasars at $0.1 < z < 5.2$ (Richards et al. 2006), as well as the quasars in our sample, have redder optical–mid-infrared colors ($r - m_{3.6\mu m} > 0.35$, shown as a large ellipse) than stars with similar optical colors. We also examined the robustness of star selections by comparing the star count in the V band with that predicted by the Besançon model. Stars in the SXDF were selected from the catalogs using the same criteria as for the variable objects. Star counts including reliable stars, probable stars, and possible stars in the SXDF reasonably agree with the model prediction in $21 < V < 24$. In the bottom right panel of Figure 7 there are several $R - i > 0.6$ point sources with stellar optical–mid-infrared colors and low color scores $c_{\rm score}$ on the stellar sequence (gray circles below the dot-dashed line). These low color scores may derive from nonsimultaneous observations[22] and their variability. In this way, our classifications based on colors of objects could be inaccurate because of nonsimultaneous observations, but many points detailed above indicate that variable stars are securely selected through our criteria, with small contamination and high completeness. The reliable stars, probable stars and possible stars, 107 objects in total (0.889 deg^2, 120 objects deg^{-2}), make up our sample of variable stars in subsequent discussions.

[22] For example, V-band observations have been mainly carried out after those in other broad bands were almost finished (Furusawa et al. 2008).

4.2. *SN/AGN Separation*

After we selected variable stars, we classified nonstellar variable objects into SNe and AGNs based on two parameters from the optical imaging data: the offset of the location of the variable component from the host object, and the light curve.

4.2.1. *Criteria for the Variable Location*

First, we examined the offsets between the variable components and their host objects. Variability should be observed at the centers of the host objects for AGNs as well as stars, while SNe can explode at any position relative to the host objects. In order to estimate the errors of the locations of variable components for AGNs, we examined the offsets for optically variable X-ray sources. Most of the X-ray sources are considered to be AGNs. Some of them can be stars emitting X-rays, but for our purposes, that is not a problem: variable stars should also show variability at their centers. Almost all of the X-ray-detected variable objects ($\sim$97%) have spatial offsets below 1 pixel (0.202″), and the offsets distribute with a scatter of $\sigma_{\rm offset,X\text{-}ray} = 0.29$ pixel. We also examined

offsets for simulated variable objects used in calculations of detection completeness in § 5, and found that their offsets from the located positions range with a scatter of $\sigma_{\rm offset,\,sim} = 0.51$ pixel, slightly larger than that of X-ray sources. We set the threshold between *central variability* (variability at the central positions) and *offset variability* (variability at the offset positions) to 1.2 pixel, which is $3\sigma_{\rm offset}$ (using the average of these two error estimates).

4.2.2. *Criteria for the Light Curve*

We also used light curves to discriminate SNe from AGNs. Bright phases where we detect object variability should be limited to within 1 yr for SNe, for two reasons. First, multiple SNe very rarely appear in a single galaxy within our observational baselines. Second, any SNe should become fainter than our detection limit within 1 yr after the explosions in the observed frame. SNe Ia, the brightest type except for hypernovae and some of Type IIn SNe, can be seen at $z \sim 1.4$ at our detection limit ($i'_{\rm vari} \sim 25.5$ mag). One year in the observed frame corresponds to 5 months in the rest frame at $z = 1.4$ due to the time dilation by cosmological redshift. Therefore, SNe should fade by more than 4 mag below the maximum brightness (e.g., Jha et al. 2006). This decrease of brightness is a minimum value of observed declining magnitudes of SNe and is almost the same as the dynamic range of our detection for variability ($i'_{\rm vari} = 20.5$–25.5 mag). Hence, we defined objects that are at bright phases for less than 1 yr, and are stably faint in the remainder of the observations, as "objects with SN-like light curves." In order to apply this criterion for the variable objects, it is necessary for light curves to cover more than 3 yr at least. In two fields (SXDF-N and SXDF-W), our images cover only 2 yr, 2002 and 2003; therefore, variable objects in these two fields cannot be classified as like or unlike SNe. Hence, we concentrate on the other three fields (SXDF-C, SXDF-S, and SXDF-E) to discuss number densities of SNe and AGNs based on robust classifications. Among 693 variable objects in these three fields, 619 objects are classified as nonstellar objects. Out of 619 nonstellar variable objects, light curves of 27 objects cover only 2 yr because of insecure subtractions in some epochs. Therefore, we use 592 objects in the following section when separating SNe from AGNs. The number densities derived below can increase by a factor of 1.05 (619/592) to account for the objects lost to poor subtractions. We also note that these criteria provide misclassifications for objects with light curves with poor signal-to-noise ratios.

4.2.3. *Results of SN/AGN Separation*

We combined these two criteria, the position offsets and the light curves, and applied them to 592 objects over 0.566 deg^2 in order to classify variable objects as SNe and AGNs. Variable objects with significant (>1.2 pixel) offsets and SN-like light curves (case 1, 158 objects) are highly likely to be SNe, while those with small ($\leq$1.2 pixel) offsets and non-SN-like light curves (case 2, 228 objects) are highly likely to be AGNs. There are no clear contaminations in either case in our sample; we have no X-ray sources or spectroscopically identified broad-line AGNs classified as case 1, and also have no SNe with spectroscopic identifications or spectroscopic redshift determinations of their host galaxies in Yasuda et al. (2008, in preparation) classified as case 2.

Objects with small offsets and SN-like light curves (case 3, 160 objects) or significant offsets and non-SN-like light curves (case 4, 46 objects) are hard to judge. In our time samplings and baselines, AGNs can be classified as SNe in terms of light curves, and objects in case 3 can be either SNe or AGNs. Out of 14 SNe with spectroscopic identifications or spectroscopic redshift determinations of their host galaxies, 8 objects are classified as case 1 (significant offsets and SN-like light curves), and 5 objects are classified as case 3 (small offsets and SN-like light curves). Only 1 object is classified as case 4 (significant offsets and non-SN-like light curves), probably because the variable component of this object is the faintest among these 14 SNe ($i'_{\rm vari} = 25.3$mag). Through our criterion for offsets of variability, 36% (5/14) of SNe are recognized as central variability, although spectroscopic observations for SNe should be biased to offset variability to avoid AGNs. If we use this ratio, about 88 ($=158 \times 5/9$) of 160 objects in case 3 are considered to be SNe. On the other hand, among 644 variable objects in these fields whose light curves cover longer than 3 yr, the number of X-ray sources is 128. Out of 128 optically variable X-ray sources (which we believe are AGNs), 89 objects are in case 2, 37 objects are in case 3, 1 object is in case 1, and 1 object is in case 4. Thus, 30% [$=(37+1)/128$] of AGNs have SN-like light curves. If we assume that this same fraction of all AGNs have SN-like light curves, then about 96 [$=228 \times (37+1)/(89+1)$] of 160 objects in case 3 are considered to be AGNs. The expected total number of these SNe and AGNs in case 3 is 184 ($=88+96$), reasonably consistent with the real number (160) in case 3. Hence, we made number densities of SNe and AGNs by scaling those for well-classified samples (case 1 for SNe and case 2 for AGN) by factors of 14/8 for SNe and 128/89 for AGNs, as shown in Figure 12 for the host object magnitudes and Figure 13 for the variable component magnitudes. We discuss these figures in § 6. We obtained these number densities of 489 and 579 objects deg^{-2} for SNe and AGNs, respectively.

The nature of objects in case 4 is mysterious. We have only two spectroscopic data for objects in case 4, and both spectra indicate that they are normal galaxies at $z \sim 0.5$. Their offsets from the centers of the host objects are significant. The light curves have marginal parameters around the threshold between those of SN-like light curves and non-SN-like light curves, and they may be misclassified as non-SN-like light curves due to measurement errors. On the other hand, only one object in case 4 is detected in X-rays. This object and some others have offsets from the centers of their host galaxies just above the threshold (1.2 pixel). Another possible reason for the classification of some objects as case 4 is misidentifications of the host objects due to faintness. Such objects might be also transient objects. The number of objects in case 4 is not large, and we do not include them in discussions of number densities.

5. DETECTION COMPLETENESS OF OPTICALLY VARIABLE OBJECTS

We intensively studied two types of completeness in this paper. One is completeness of the variability detection itself, which should be functions of the PSF size and background noise of the images, and should be independent of properties of object variability. Another completeness depends on behaviors of object variability and observational time samplings. It is not easy to estimate this type of completeness, because properties of variability are complicated and differ from object to object.

5.1. *Variability Detection Completeness*

The first type of completeness is simply estimated by locating artificial variable objects (point sources with PSFs of the same size as those in the real images) randomly in the stacked images using the `artdata` task in IRAF, and detecting them in the same manner as for the real images. Three examples are shown in Figure 8. We can almost completely detect variable objects whose flux differences are brighter than $\sim$25.0–25.4 mag. The cutoffs at the bright ends around $i'_{\rm vari} = 20.0$–20.5 mag are caused by masking bright objects to avoid false detections of variability.

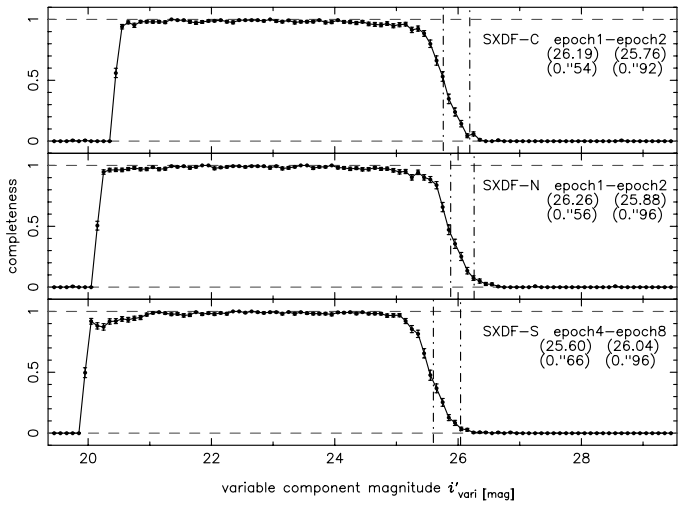

FIG. 8.—Detection completeness of variable objects as a function of variable component magnitude i'_{vari}, calculated by adding artificial objects to the images and detecting them in the same manner as for the real images. Three cases are shown in the figure. The limiting magnitudes of the images before subtractions are given between the top parentheses and shown by dot-dashed lines. FWHM of PSF are also described between the bottom parentheses. Cutoffs at bright magnitudes are caused by masking bright objects so that our detection are not affected by saturation or nonlinearity of the CCD pixel.

The detection completeness decreases down to zero at $i'_{vari} \sim 26.0$–26.3 mag. The shapes of completeness curves are similar for all the subtracted images, although there are slight offsets in magnitude axis due to differences of limiting magnitudes of the stacked images. The completeness is almost uniform in the whole regions of the subtracted images where we investigate object variability.

5.2. *Detection Completeness for Variable Stars, SNe, and AGNs*

Variability detection completeness depends on the shapes of light curves of variable objects and observational time samplings. We want to know the detection completeness for each class of variable object. This is difficult to ascertain for objects showing burst-like variability, such as dwarf stars, SNe, and AGNs, while we can easily simulate light curves of pulsating variable stars showing periodic variability. AGN optical variability has been often characterized by the structure function (Kawaguchi et al. 1998; Hawkins 2002; de Vries et al. 2003, 2005; Vanden Berk et al. 2004; Sesar et al. 2006), and we can simulate AGN light curves to estimate the detection completeness. Hence, we consider two types of simulated light curves: periodic variability for pulsating variable stars, and variability characterized by structure functions for AGN, and estimate completeness. We also evaluate the variability detection efficiency using real light curves and the X-ray source sample for AGNs.

In our time samplings and depths, SNe Ia up to $z \sim 1.4$ can be detected with an efficiency of a few tens of percent. The detection efficiency for SNe will be examined in detail in a forthcoming paper on the SN rate.

5.2.1. *Periodic Variability*

The detection completeness for pulsating variable stars whose variability is periodic is easily calculated. Simulated light curves are parameterized by magnitude amplitudes $A = 0.0$–1.0 mag, periods $T = 0.01$–20000 days, and averaged magnitudes $m_0 = 21$–26 mag.[23] We have roughly two types of time baselines of observations, and then we show the completeness for the two fields, SXDF-C with observations from 2002 to 2005, and SXDF-N with observations from 2002 to 2003, in Figure 9. There are slight differences between the detection completeness for the two fields, but they are almost the same on the whole. In all five fields, some dark spikes indicating low sensitivity to those periods can be seen, because our observations have been carried out only in autumn. The completeness is a strong function of magnitudes and amplitudes. We can detect only variable stars with large amplitudes ($A > 0.4$ mag) for faint stars of $i' > 24$ mag.

[23] Light curves are expressed as $m(t) = (A/2)\sin(2\pi t/T) + m_0$.

5.2.2. *AGN Variability*

Unlike pulsating stars, AGNs usually show burst-like variability aperiodically. The behavior of AGN variability depends on rest-frame wavelength. Generally, AGN variability is larger at shorter wavelengths. Considering the time dilation of cosmological redshift, the detection efficiency of AGNs by optical variability in a certain broad band, the i'-band in this study, is not clear. To zeroth approximation, the effects of wavelength dependence and time dilation cancel each other.

Quasar variability has been often described in the form of the structure function,

$$\mathrm{SF}(\Delta t) \equiv \left\{ \sum \frac{[m(t+\Delta t) - m(t)]^2}{N(\Delta t)} \right\}^{0.5}, \qquad (1)$$

where $N(\Delta t)$ is the number of objects with time intervals of Δt. Since focus on timescales of months to several years (not several decades), a power-law form of the structure function, $\mathrm{SF}(\Delta t) = (\Delta t/\tau_0)^{\gamma}$, parameterized by a characteristic timescale of variability, τ_0, and a power-law slope, γ, is well fitted to observational data. The structure function begins to show a turnover around the rest-frame time lag of a few years, and this power-law approximation slightly overestimates the variability (Ivezić et al. 2004b; de Vries et al. 2005; Sesar et al. 2006). However, our observational data span over only 3 years at longest in observed frame, and this simplification is good enough for our estimation of AGN detection completeness.

The slope of the structure function provides an important key to the origin of their variability (Hughes et al. 1992; Hawkins 1996, 2002; Kawaguchi et al. 1998) in accretion disk instability (Rees 1984), bursts of SN explosions (Terlevich et al. 1992), and microlensing (Hawkins 2002). Therefore, the slope of structure function has been investigated in many previous studies. Monitoring observations of Palomar-Green (PG) quasars (Giveon et al. 1999; Hawkins 2002) and variability studies of enormous numbers of SDSS quasars between SDSS imaging data and older plate imaging data (de Vries et al. 2003, 2005; Sesar et al. 2006), or SDSS spectrophotometric data (Vanden Berk et al. 2004) have set constraints on characteristic behaviors of variability. They obtained slopes of $\gamma \sim 0.2$. We simulated light curves satisfying the structure function with $5 \times 10^4 < \tau_0 < 1 \times 10^6$ days and $0.05 < \gamma < 0.6$ for averaged apparent magnitudes $m_0 = 21$–26 mag for AGN components, and calculated detection completeness in our observational time samplings. We show results in Figure 10 for two cases (4 year baseline for SXDF-C, S, and E, and 2 year baseline for SXDF-N and W) for periodic variability explored in § 5.2.1. Values of the slope obtained in previous studies indicate that the main origin of AGN optical variability is accretion disk instability or microlensing, and the typical values of τ_0 and γ are $\sim 6 \times 10^5$ days and ~ 0.2 in observed frame, respectively, which are indicated as stars in Figure 10. These values were derived from

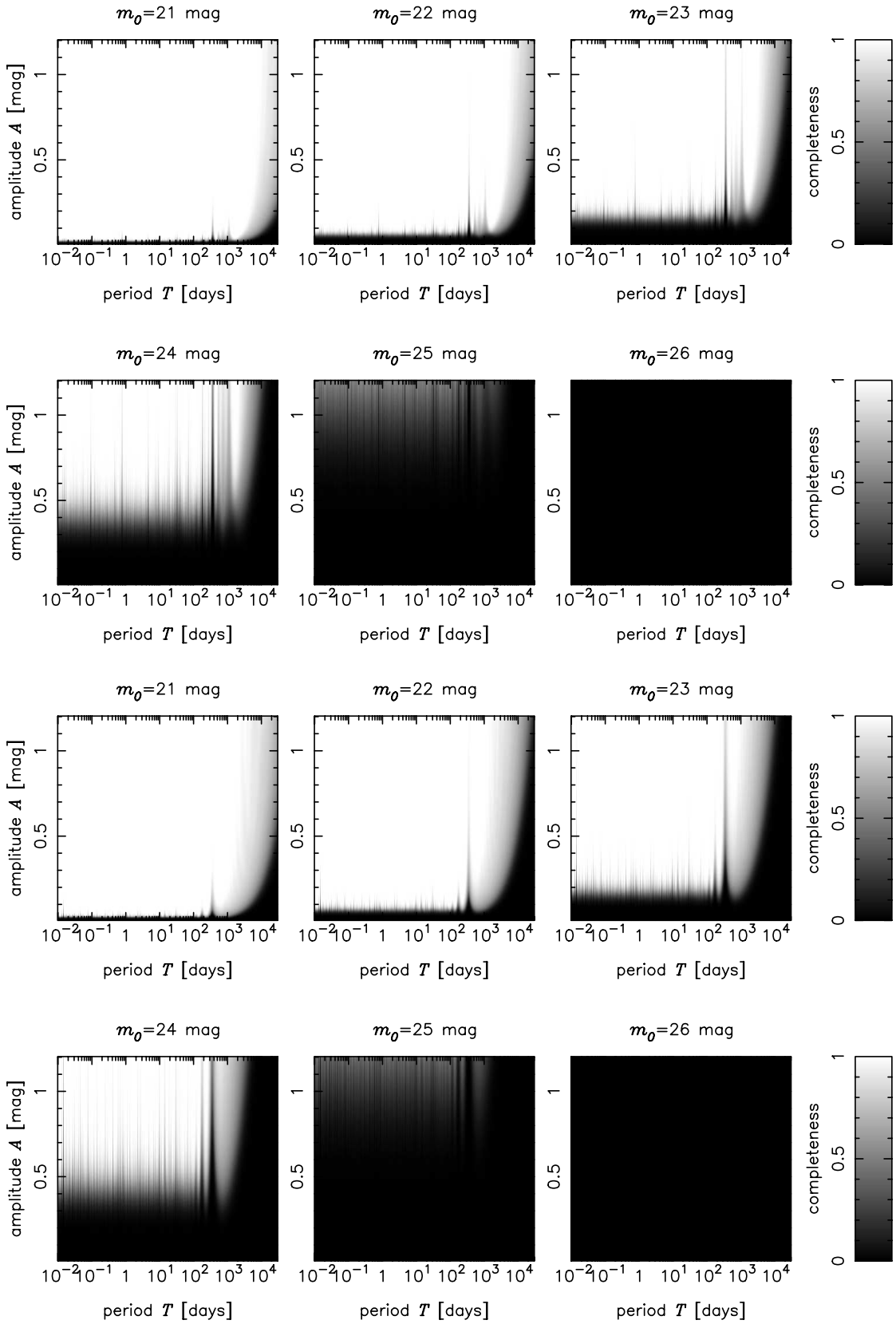

FIG. 9.— Detection completeness for variable objects showing periodic variability with periods T, amplitude A, and averaged magnitude m_0 in SXDS-C (10 epochs from 2002 to 2005; top six panels) and SXDS-N (8 epochs from 2002 to 2003; bottom six panels).

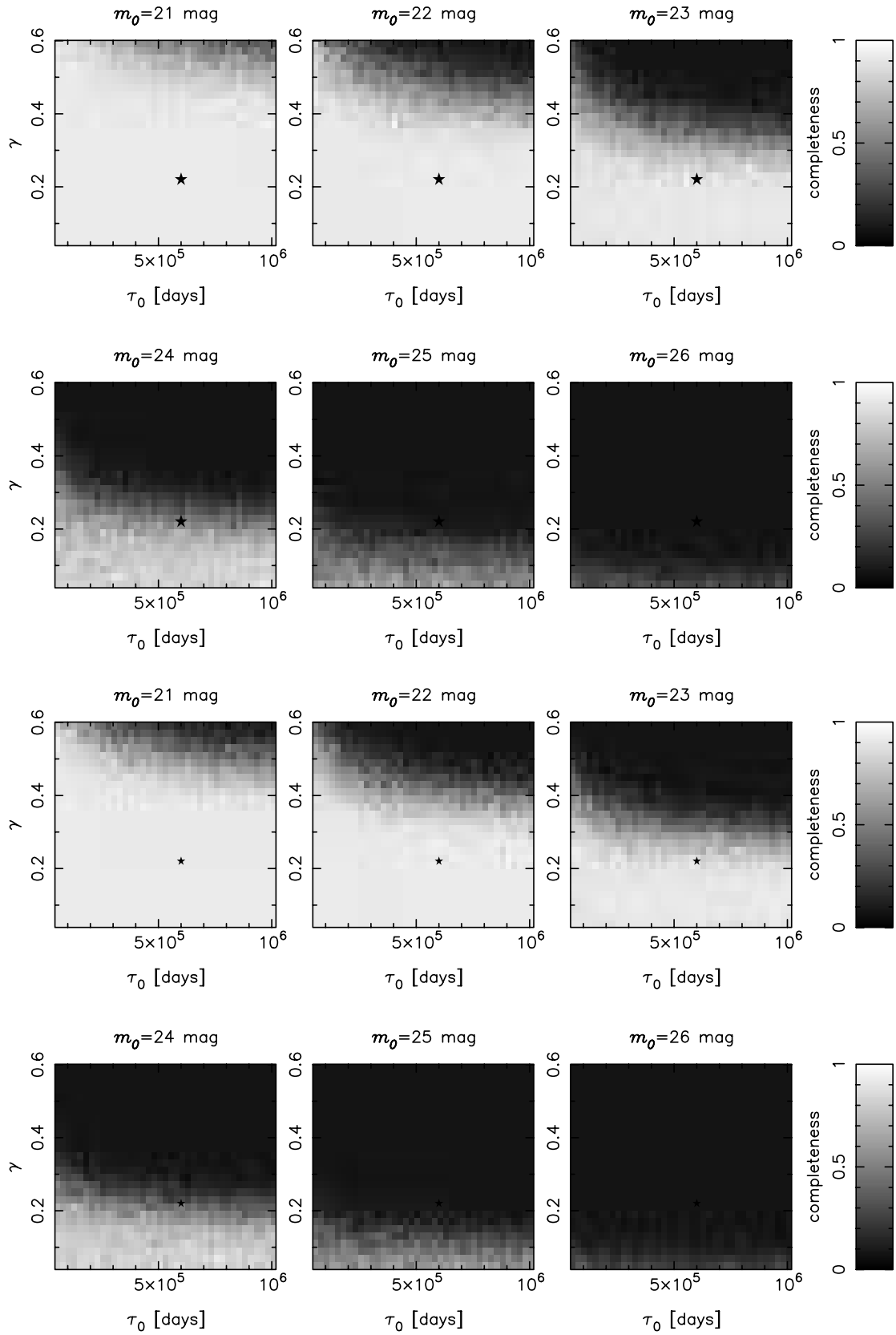

FIG. 10.— Detection completeness for variable objects whose variability are characterized by the structure functions in SXDS-C (10 epochs from 2002 to 2005; top six panels) and SXDS-N (8 epochs from 2002 to 2003; bottom six panels). Typical values of γ and τ_0 for quasars are 0.2 and 6×10^5 days, respectively; these values are plotted as stars.

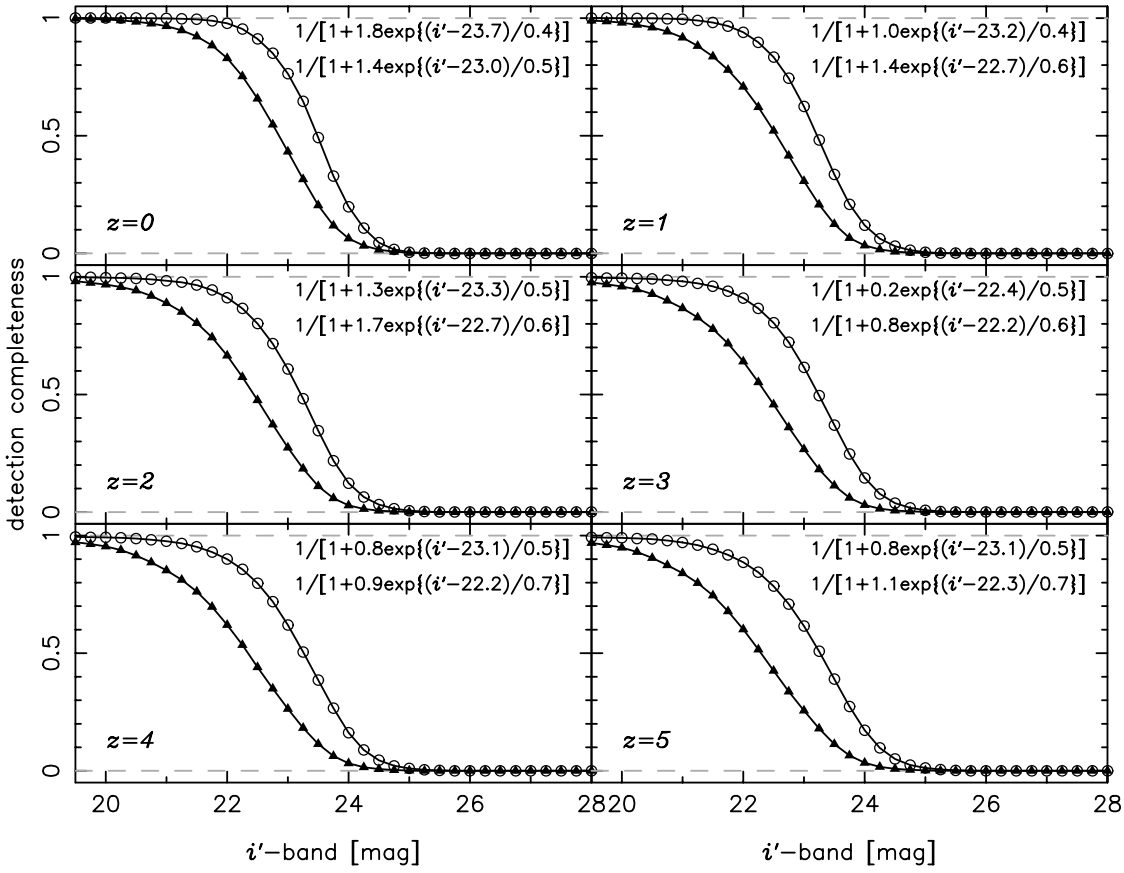

FIG. 11.—Detection completeness for 42 PG quasars using real light curves over 7 years obtained by Giveon et al. (1999). In the cases of objects at $z = 0, 1, 2, 3, 4$, and 5, we calculated the detection completeness considering cosmological time dilation and variability dependence on rest-frame wavelength (Vanden Berk et al. 2004). We show the results for time samplings in SXDF-C as open circles, and for those in SXDF-N as filled triangles. The fitted lines are $1/\{1 + a \exp[(\mathrm{mag} - b)/c]\}$, parameterized by a, b, and c.

observations in bands bluer than the i'-band used in this work. In i'-band, it is expected that γ stays roughly constant and τ_0 become slightly larger. Determination errors of τ_0 and γ are not small here, and we infer that the completeness for our data is not less than $\sim$50% for $m_0 < 24$ mag.

The detection completeness for quasars was also estimated using observational light curves of 42 PG quasars in B and R bands over 7 years obtained by Giveon et al. (1999). The photometric points were well sampled, and their observational time baselines are much longer than ours. They lacked time samplings on timescales of days, and we interpolated the light curves. Their quasars are at relatively low redshift ($0.061 < z < 0.371$), with luminosity of $-26.3 < M_B < -21.7$ mag. The well-sampled light curves are very useful for calculating the completeness in our survey. In our estimations of the detection completeness, we assume the photometric errors of our surveys, considering the time dilation and dependence of variability on rest-frame wavelength, which was indicated in Vanden Berk et al. (2004) using the SDSS quasars. Variability depends on rest-frame wavelength, and quasars are about twice as variable at 1000 Å as at 6000 Å, as shown in their equation (11) [24] and their Figure 13. We obtained detection completeness curves as a function of observed i'-band magnitude, as shown in Figure 11. From top left to bottom right, the redshifts are $z = 0, 1, 2, 3, 4$, and 5. The results for the two fields, SXDF-C from 2002 to 2005 and SXDF-N from 2002 to 2003, are plotted. There are some differences between these cases, and the longer baselines give us higher completeness. In this simulation, our detection completeness for AGNs is down to zero at $\sim$24.5–25.0 mag. The redshift dependence of the completeness is very small due to cancellation of time dilation and the dependence of variability on rest-frame wavelength. We note that the dependence of variability on AGN luminosity is not considered. In our detection limit, we can observe Seyfert-class AGNs at low redshift, and our estimates of completeness here may be a lower limit for them, because of the anticorrelation between AGN luminosity and variability.

Optical variabilities of 172 X-ray sources are detected, while we have 481 X-ray sources in our variability survey field. The fraction of objects showing optical variability among X-ray sources is $36\% \pm 2\%$. All of the X-ray-detected variable objects are brighter than $i' = 24.4$ mag. When we also limit X-ray sources to those with $i' < 24.4$ mag, the number is 334. Simply assuming that all the X-ray sources can show large enough variability to be detected, the detection completeness for X-ray sources is $51\% \pm 3\%$. Vanden Berk et al. (2004) found that X-ray-detected quasars show larger variability than quasars that are not detected in X-rays. This tendency is true for our sample; X-ray brighter sources show larger optical variability than X-ray fainter sources in a certain optical magnitude. Variable objects not detected in X-ray should have lower completeness than variable objects detected in X-rays. Some of the X-ray sources are Type 2 populations whose optical variability are more difficult to detect given the unified scheme of AGNs, and the detection completeness of Type 1 AGNs can be higher than these estimates.

These three estimations of detection completeness for AGNs are roughly consistent with each other and strongly depend on

[24] Variability $v(\lambda)[\mathrm{mag}] = 0.616 \exp(-\lambda/988\ \text{Å}) + 0.164$.

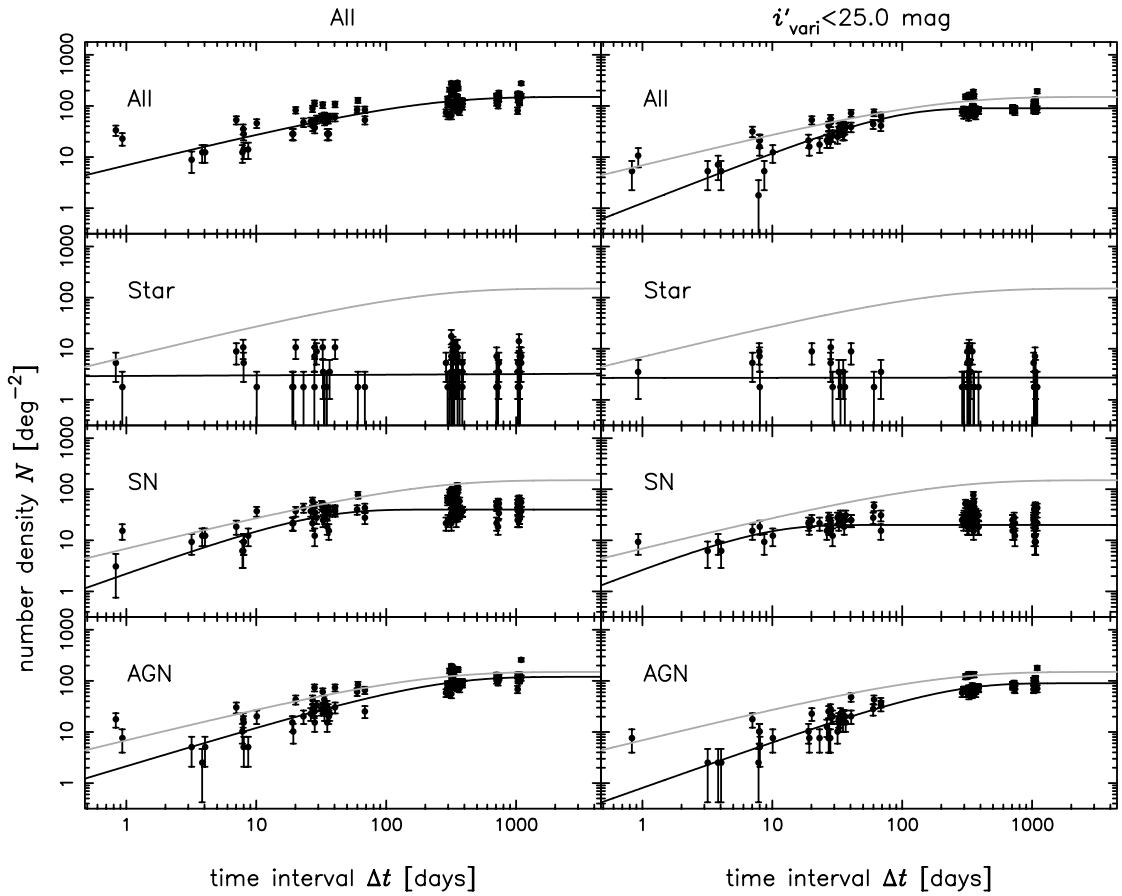

FIG. 12.—Number densities of variable objects as a function of time intervals of Δt in i'-band imaging observations. We plot them for objects showing variability above 5 σ_{lc} in the left column, and for objects with variable component magnitude i'_{vari} brighter than 25.0 mag in the right column. These points are fitted in the form of $N = a \times \exp[-b(\Delta t)^c]$ (*solid lines*). The fitted line in the top left panel is shown as a gray line in every panel as a reference.

apparent magnitudes as well as pulsating variability. The inferred completeness is ~1 at $i' \sim 21$ mag and slowly decreases down to zero at $i' = 24$–25 mag, with uncertainty of a factor of a few.

6. OVERALL SAMPLE

We found 1040 variable objects, including possible transient objects, in the i'-band in the SXDF down to variable component magnitudes of $i'_{vari} \sim 25.5$ mag. In the top left panel of Figure 12, the number densities N of all the detected variable objects are shown as a function of time interval Δt of observations when we compare only two separated images. We also draw a line fitted in the form of $N(\Delta t) = a\{1 - \exp[-b(\Delta t)^c]\}$ Number densities as a function of Δt for SNe are expected to bend over at a certain time interval, because variability timescales of SNe are roughly common to each other, a few months in rest frame. Then, we introduce such function forms for all the kinds of variable objects. Detection limits for variable objects are slightly different for each combination of observational epochs, and this can affect the number densities obtained. We also show number densities of variable objects with variable components brighter than 25.0 mag in the right panels of Figure 12. Monotonic increases of number density in the observed frame indicate that objects showing variability on timescales of years are dominant in this magnitude range (and in the SXDF direction, the Galactic halo). The number densities for variable stars are shown in the second row, with SNe in the third row, and AGNs in the bottom row, after classifying variable objects in § 4. Variable objects used for calculating number densities in this figure are 644 objects with light curves in long baselines from 2002 to 2005, enough to discriminate SNe from AGNs, and all are within the IRAC field. These SN and AGN number densities are corrected for case 3 objects. Typical timescales of variability are from days to months for variable stars and SNe, while AGNs show variability on timescales of months to years (e.g., Vanden Berk et al. 2004). The flat distributions for variable stars indicate that stars showing variability on short timescales are mainly included in the sample. The SN number densities arrive at a plateau on timescales of about a few months, as expected from timescales of SN light curves. On the other hand, significant increases toward timescales of years are seen for AGNs. Fitted lines for AGNs in the same form as the function for SNe show possible turnovers at $\Delta t \sim 1000$ days. Results for SDSS quasars (Ivezić et al. 2003) indicated turnovers of the structure function at $\Delta t \sim 1000$ days in rest frame, and these possible turnovers in our results may be real. These results indicate that long time baselines of years make the completeness significantly higher only for AGNs.

We show the number densities of variable objects as a function of variable component magnitude i'_{vari} in the left column of Figure 13. Number densities after classifying variable objects into variable stars, SNe, and AGNs in three timescales, $\Delta t < 10$ days in the second column, $10 < \Delta t < 50$ days in the third column, $50 < \Delta t < 200$ days in the fourth column, and $\Delta t > 200$ days in the right column, are also plotted. All the number densities drop around $i'_{vari} \sim 25$ mag, and our variability detections are reasonably consistent with simulated completeness, as shown in Figure 8. In the bottom row of Figure 13, the number densities of transient objects are plotted. By the definition of transient objects (see § 4), their variable component magnitudes correspond to total magnitudes in their brighter phases. The transient object sample

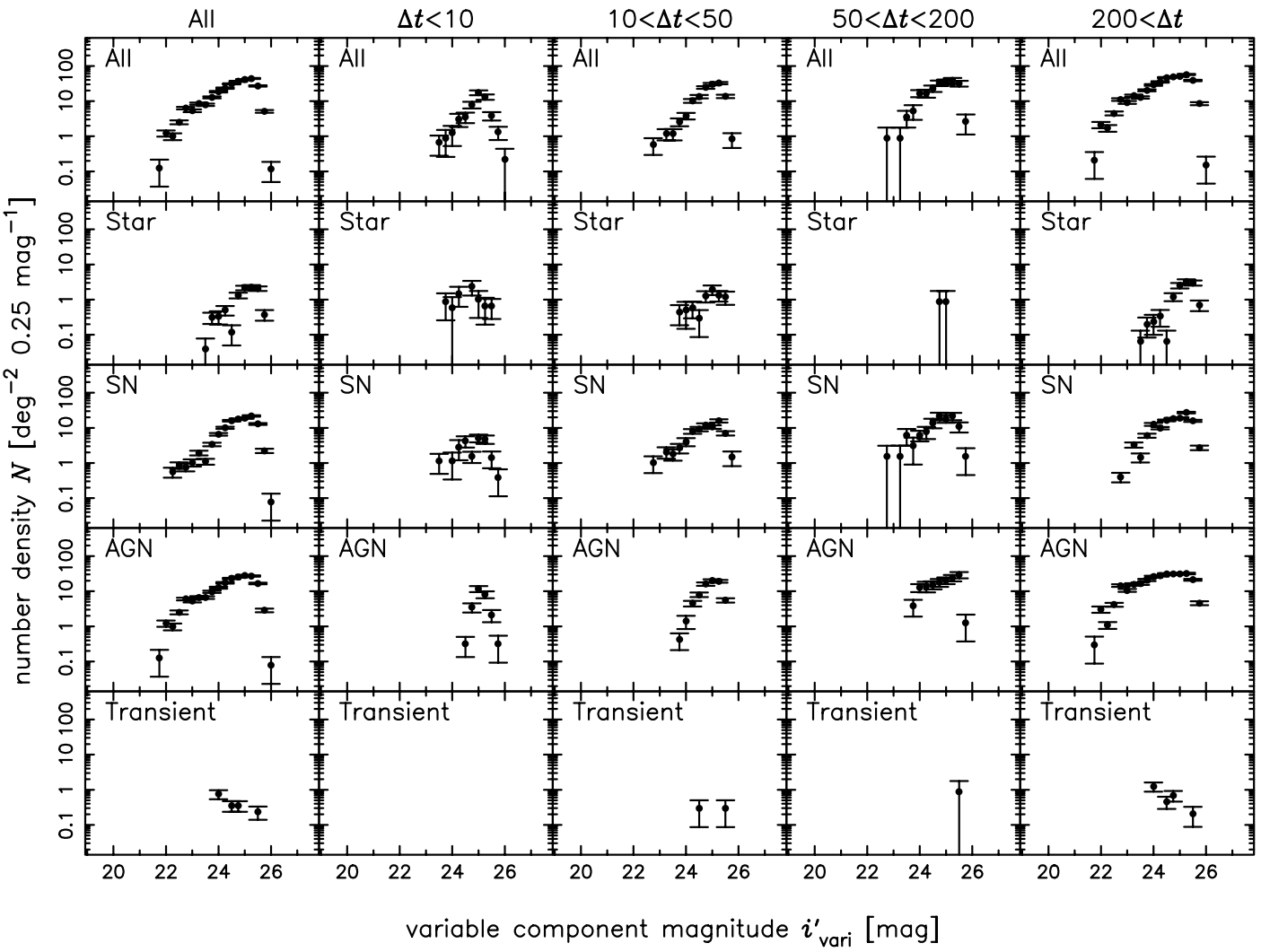

FIG. 13.—Number densities of variable objects as a function of variable component magnitude $i'_{\rm vari}$, plotted for (*rows, top to bottom*) all the variable objects (*top row*), variable stars, SNe, AGNs, and possible transient objects (*bottom*), and for (*columns, left to right*) all the observational data (*left*), and timescales $\Delta t < 10$ days, $10 < \Delta t < 50$ days, $50 < \Delta t < 200$ days, and $\Delta t > 200$ days (*right*).

can include not only objects showing transient phenomena such as flare-ups of faint dwarf stars, but also Kuiper belt objects moving less slowly than $\omega \sim 1''$ hr^{-1} (a typical value of seeing size per exposure time for each stacked image), corresponding to a semimajor axis of >100 AU. These estimates of numbers of variable objects provide the expected number of variable objects contaminating interested samples using nonsimultaneous observational data. For example, Iye et al. (2006) and Ota et al. (2007) investigated the possibility of variable object contaminations of their LAE sample at $z \sim 7.0$ in the Subaru Deep Field (SDF; Kashikawa et al. 2004), which were obtained by comparing broadband imaging data taken before 2004 with narrowband NB973 imaging data in 2005. From the bottom row of Figure 13, a few or <1 object in the SDF ($\sim$0.3 deg^2) can be just transient objects and misclassified as narrowband excess objects in their sample. Their plausible candidates with narrowband excess are 2. One of these was spectroscopically identified and turned out to be a real LAE at $z = 6.94$. Spectroscopic identification of another candidate should also be done. Whether this candidate is a real LAE or not, the number of narrowband excess objects they found is consistent with the number expected from statistics of number densities of transient objects.

The fraction of variable objects of the overall objects in the SXDF are shown in Figure 14. Magnitudes used in this figure are the total magnitudes of host objects. About 5% of the objects at $i' \sim 21$ mag show optical variability, and the fraction rapidly decreases toward fainter magnitudes. These declines are caused by the detection limit for variability. Large variability relative to the host object is necessary for faint objects to be detected. Almost all of objects in the SXDF are galaxies, not stars (the fraction of stars is $\sim$4%). Then, the fraction of variable AGNs is $\sim$3% around $i' \sim 21$ mag, where the detection completeness is $\sim$1. Sarajedini et al. (2006) found that 2.6% of galaxies have variable nuclei down to $V_{\rm nuc} < 27.0$ mag without completeness corrections using two-epoch observations separated by 7 years. Their fraction is consistent with ours. Cohen et al. (2006) also used four-epoch ACS imaging data on time baselines of 3 months down to $V_{\rm total} < 28$ mag and detected variability of $\sim$1% of galaxies. This small percentage in Cohen et al. (2006) is consistent with ours if we consider their short time baselines, since most AGNs vary in brightness on longer timescales of years, as shown in Figure 12.

7. VARIABLE STARS

The sample of variable stars used in this section includes 153 objects which were classified as reliable stars, probable stars, and possible stars in § 4.1. The top panels of Figure 15 show color-magnitude diagrams of i' versus $R - i'$ (*left*) and V versus $B - V$ (*right*) for variable stars (*black circles*) and nonvariable stars in the SXDF (*gray dots*).

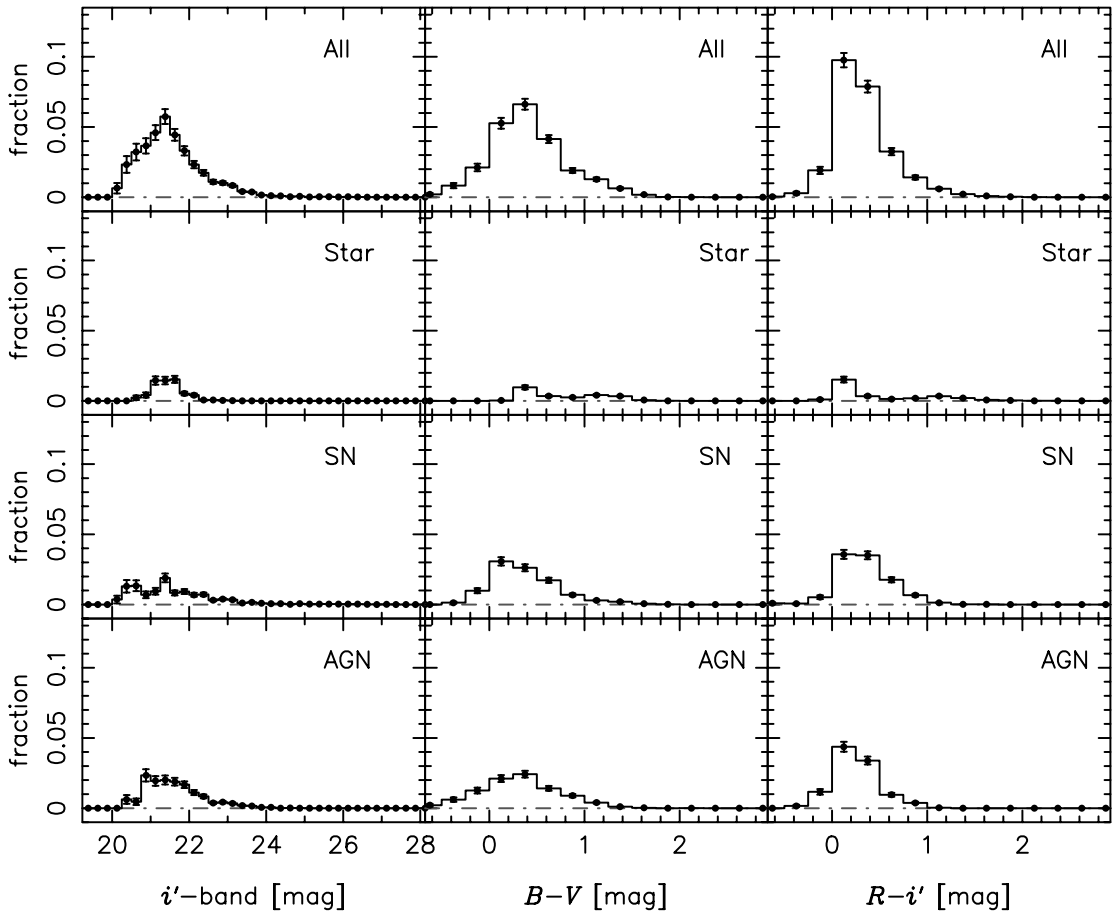

FIG. 14.—Fractions of all the variable objects to the whole set of objects in the SXDF as functions of i'-band magnitude, $B - V$, and $R - i'$ colors (*top row*). Fractions after classifying variable objects are also plotted in the second, third, and bottom rows.

These nonvariable stars are selected through the same criteria as the variable stars. Number counts and fractions of variable stars are also plotted in the rows below. Figure 16 shows color distributions and fractions of variable stars for $R - i'$ and $B - V$. The number count in the i'-band has a relatively steep peak at $i' \sim 21.5$ mag, and decreases toward fainter magnitudes. This cutoff is partly caused by the variability detection limit. The dot-dashed lines indicated in the left columns of Figure 15 are total magnitudes of objects with variable components of the detection limit, $i'_{\rm vari} \sim 25.5$ mag, in the cases of variability amplitudes of 0.05, 0.1, and 0.3 mag (*left to right*). Thus, limiting magnitudes can be as shallow as ~22.2 mag for variable objects with low variability amplitudes of ~0.05 mag. Poor time samplings of our observations prevent us from determining amplitudes of variability in cases of periodic variability. Assuming that amplitudes roughly equal magnitude differences of objects between their maxima and minima in our samplings, the amplitudes of almost all of variable stars are less than 0.1 mag, as shown in Figure 17. These variable stars with low amplitudes can be detected above ~22.2 mag. Variable stars with larger amplitudes can be detected for fainter stars. The top right panel of Figure 17 clearly indicates this tendency of variability selection effects.

Bimodal distributions are clearly seen in the figures of color-magnitude diagrams (Fig. 15) and color distributions (Fig. 16); there are two populations of blue bright ($V \sim 22$ mag) variable stars and red faint ($V \sim 23.5$ mag) variable stars. From comparison with the Besançon model prediction, stars in the upper sequence belong to the thick disk rather than thin disk populations, because the stellar sequence of the thin disk is expected to be redder than the observed sequence by $B - V$ of ~0.3. The red variable stars are considered to be dwarf stars showing flares or pulsating giant stars. On the other hand, stars in the lower sequence belong to the halo populations. The blue variable stars are considered to be pulsating variable stars, such as δ Scuti, RR Lyrae, and γ Doradus stars, within the instability strip in color-magnitude diagrams. Eclipsing binaries may be also included.

Ivezić et al. (2000) selected RR Lyrae candidates using SDSS multiepoch wide-field imaging data on short timescales of days, and found a cutoff magnitude at $r^* \sim 21$ mag. They indicated that this cutoff magnitude corresponds to a distance of ~65 kpc from the Galactic center, which might be the edge of the Galactic halo. Our time samplings are too poor to determine their periods of variability as well as real amplitudes. Maxima of magnitude differences in our time samplings shown in Figure 17 are expected to be smaller than real amplitudes by a factor of ~1.2 from simulated light curves. Our typical exposure time of 1 hr, which is not much longer than variability periods of RR Lyrae (0.3–0.6 days; Vivas et al. 2004), also makes these magnitude differences small. Moreover, variability in the i'-band is smaller than that in the V-band for RR Lyrae (0.5–1.0 mag in V-band; Vivas et al. 2004) by a factor by ~1.5 (interpolation of values in Table 7 of Liu & Janes 1990). In total, the maxima of magnitude differences in the i'-band are expected to be less than 0.2–0.5 mag for RR Lyrae in our time samplings. Given the variability amplitudes of blue variable stars with $B - V \sim 0.3$ in our sample, there are one or a few RR Lyrae candidates with amplitudes as large as RR Lyrae (see bottom left panel of Figure 17). The variability amplitude of the spectroscopically identified blue variable star with $B - V = 0.44$

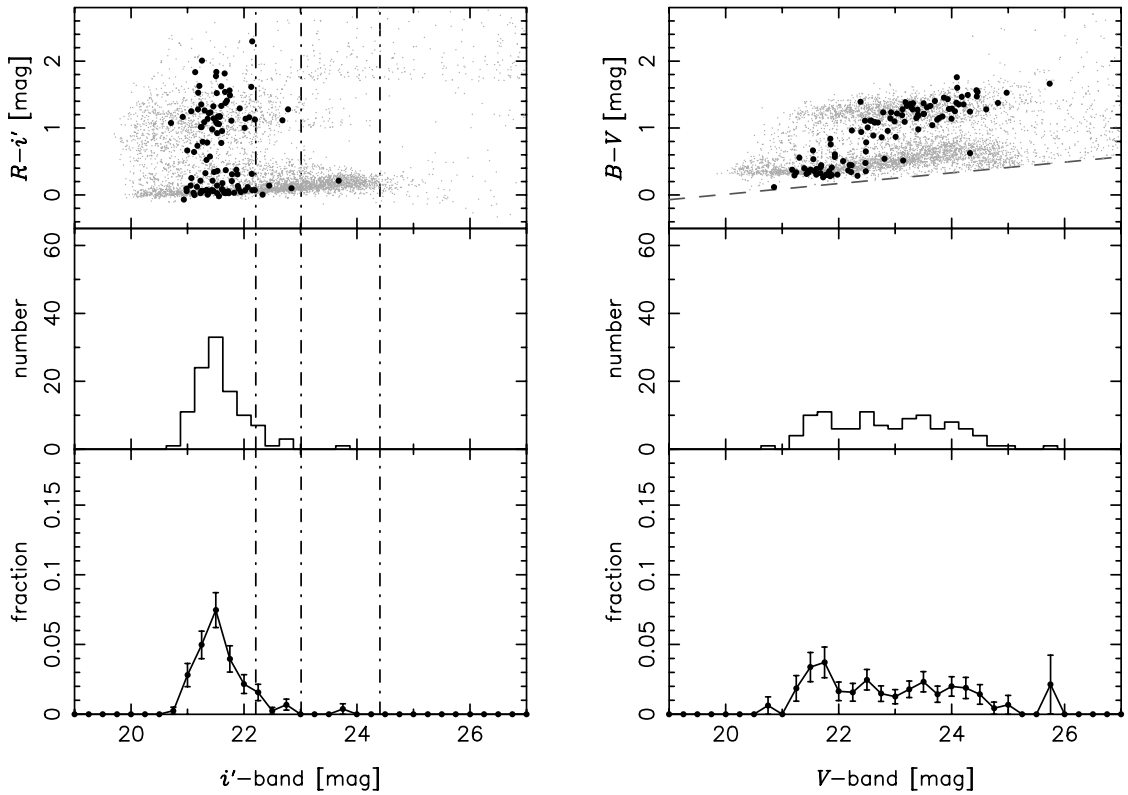

FIG. 15.— *Top*: Distributions of variable objects (*black circles*) in color-magnitude diagrams V vs. $B - V$ (*left*) and i' vs. $R - i'$ (*right*). Nonvariable stars are also shown as gray dots. The criterion for excluding contaminations of galaxies, $B - V > 0.08V - 1.59$, is shown as a dotted line in the V vs. $B - V$ diagram. Number counts and fractions of variable objects for i' and V magnitudes are shown in the second and third rows, respectively.

shown in the bottom panel of Figure 3 is small, and it cannot be a candidate RR Lyrae. If these RR Lyrae candidates in our sample are really RR Lyrae stars, the distances from the Galactic center, which are calculated by apparent V-band magnitude, are larger than ∼150 kpc. The inferred number density of RR Lyrae stars is $\sim 10^{-2}$ kpc^{-3} at a distance of ∼150–250 kpc from the Galactic center toward the halo, consistent with extrapolations of results by Ivezić et al. (2000) and Vivas & Zinn (2006), in spite of our poor statistics. They are candidates for the most distant Galactic stars known so far. Other types of blue variable stars in the halo population than RR Lyraes are considered to be included in the sample, such as Population II δ Scuti stars, γ Doradus stars, eclipsing binaries, and so on. In order to examine the nature of these faint blue variable stars, dense monitoring observations for determining pulsation periods and amplitudes, and/or follow-up spectroscopic observations, are necessary.

Two of the red variable stars with $B - V = 1.36$ and 1.34 were spectroscopically observed and identified as M dwarf stars (Fig. 3). The $B - V$ colors of the red faint variable stars are ∼0.8–2.0, which indicate K or M type stars. The V-band absolute magnitudes of these stars are widely spread out; for example, $M_V =$ 8–12 mag for M stars with colors of $1.3 < B - V < 1.7$ in the case of main sequence stars from the *Hipparcos* data (Koen et al. 2002). Assuming that almost all of these red variable stars are

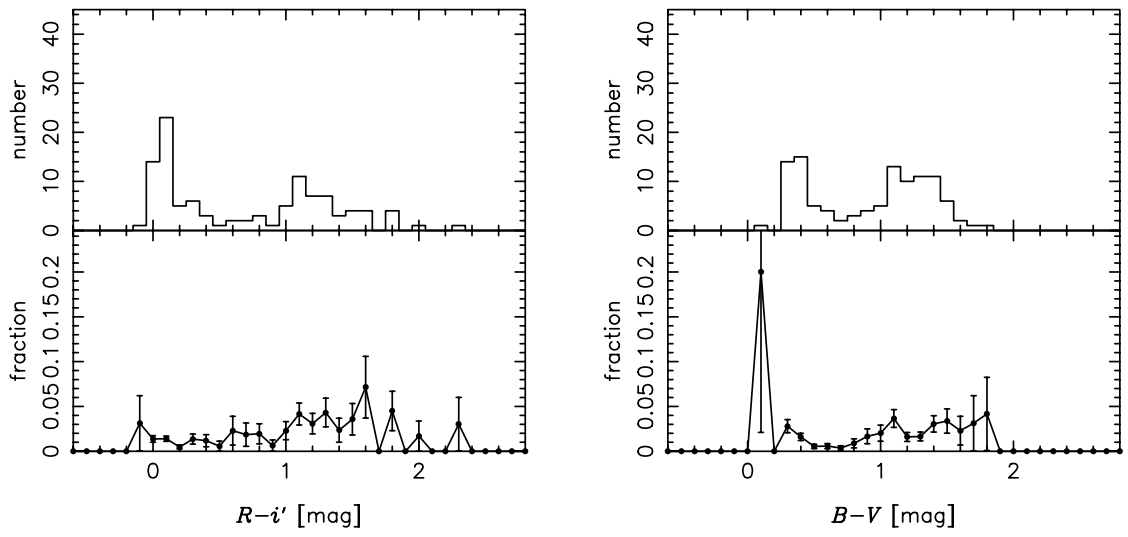

FIG. 16.— Histograms of numbers (*top*) and fractions (*bottom*) of variable objects, for $R - i'$ (*left*) and $B - V$ (*right*) colors.

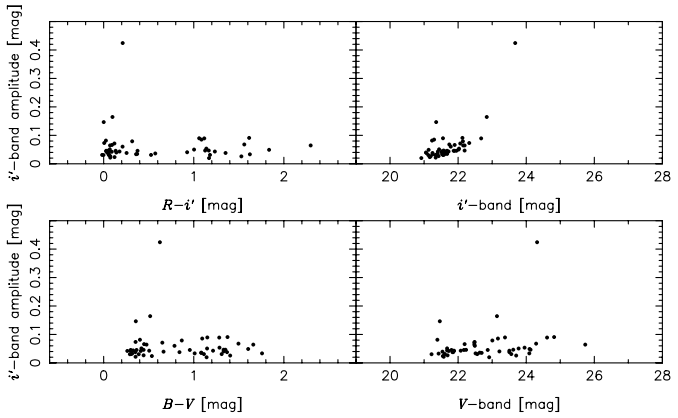

FIG. 17.— Variability amplitudes of variable stars as function of apparent magnitude (i'-band and V-band) and colors ($R - i'$ and $B - V$). These amplitudes are defined as magnitude differences between maxima and minima in our time samplings and give lower limits of real amplitudes.

dwarf stars, not red giant stars, the inferred distances to the stars are ~1.5–4 kpc from the Galactic plane, where the thick disk population is dominant (Chen et al. 2001). The number density of the variable dwarf stars is $\sim 2 \times 10^3$ kpc^{-3}. Magnitude and color distributions of stars from the model predictions are consistent with those stars in the SXDF selected using our criteria, which might indicate that a few percent of the whole population of dwarf stars show optical bursts in our time samplings, as shown in the bottom rows of Figure 16.

The fraction of variable stars is one of our interesting results. The fraction of variable stars as a function of $R - i'$ and $B - V$ color is nearly flat at a few percent, as shown in Figure 16. Tonry et al. (2005) investigated the fraction of variable stars as a function of quartile variability down to a variability of 0.015 mag. They examined the variability of stars in sequential 14 day observations down to $R \sim 20$ mag at a superb photometric precision of 0.002 mag. Their results indicate that a fraction of 0.016 mag/x of stars show variability above a quartile variability of x mag. Our detection threshold for variability of point sources corresponds to about 0.05–0.10 mag, and expected fractions are ~0.02–0.03 using this equation. The fraction obtained by our survey for blue stars is ~0.03, and for red stars is ~0.05 on average, slightly larger than the expected fraction. This discrepancy might have several causes. One young open cluster, NGC 2301, which Tonry et al. (2005) targeted, is only 146 Myr old, and should not have a significant variable population. On the other hand, our pointings are toward the halo, where the main components observed are old populations. Another reason for the discrepancy may be the difference of time samplings; their observations are 14 consecutive days, while our observations are sparse over years. The timescales that can be examined by each study are clearly different, which may also contribute to these differences. FSVS studies recently investigated fractions of faint variable stars down to $V \sim 24$ mag (Morales-Rueda et al. 2006; Huber et al. 2006). Their survey depths and directions are similar to ours, and their results for the fraction of variable stars, 5%–8% (Huber et al. 2006), are also consistent with ours.

8. SUMMARY

We have investigated the optical variability of faint objects down to $i'_{\rm vari} \sim 25.5$ mag for variable components over 0.918 deg^2 in the SXDF. Multiepoch (8–10 epochs over 2–4 years) imaging data obtained with Suprime-Cam on the Subaru 8.2 m telescope provided us the first statistical sample, consisting of 1040 optically variable objects, by image subtraction for all the combinations of images at different epochs. We classified those variable objects as variable stars, SNe, and AGNs, based on the optical morphologies, magnitudes, colors, optical–mid-infrared colors of the host objects, spatial offsets of the variable components from the host objects, and light curves. Although not all the variable objects were classified, because of short time baselines of observations in the two fields, our classification is consistent with spectroscopic results and X-ray detections.

We examined detection completeness for periodic variability and AGN variability. The completeness strongly depends on apparent magnitude. The completeness for AGNs is ~1 at $i' \sim 21$ mag and deceases down to zero at $i' \sim 24.5$ mag. Redshift dependence of the completeness calculated using light curves of PG quasar is small, due to the cancellation of time dilation and the anticorrelation between rest-frame wavelength and variability. Among X-ray sources in the field, 36% ± 2% (51% ± 3% for the bright sample with $i' < 24.4$ mag) show optical variability. Variability detections of X-ray sources also show a dependence on apparent magnitude similar to that from light curves.

Number densities of variable objects for the whole sample (variable stars, SNe, and AGNs) as a function of time interval Δt and variable component magnitude $i'_{\rm vari}$ were obtained. About 5% of all the objects show variability at $i' = 21$–22 mag, including host components, although decreasing fractions toward fainter magnitude are caused by the detection limit for variable components. The number density of variable stars as a function of time interval Δt is almost flat, indicating that the variability timescales of these stars are short. The number density of SNe arrives at a plateau on timescales of a few months, and that of AGNs increases even on timescales of years. These results are consistent with expectations from typical timescales of their variability. The total number densities of variable stars, SNe, and AGNs are 120, 489, and 579 objects deg^{-2}, respectively.

Variable stars show bimodal distributions in the color-magnitude diagrams. This indicates that these variable stars consist of blue bright ($V \sim 22$ mag) variable stars of the halo population and red faint ($V \sim 23.5$ mag) variable stars of the disk population. We selected a few candidate RR Lyrae stars, considering their large magnitude differences between maxima and minima and blue $B - V$ colors, Their number density is $\sim 10^{-2}$ kpc^{-3} at a distance of >150 kpc from the Galactic center, which is consistent with extrapolations from previous results. Follow-up observations to determine their amplitudes and variability periods might show that these candidates are at the outermost region of the Galactic halo.

Our statistical sample of optically variable objects provides us a unique opportunity to study phenomena such as AGN properties and the SN rate, which will be topics of future papers. This work also provides basic information for such future wide and deep variability surveys, such as the Panoramic Survey Telescope and Rapid Response System (Pan-Starrs; Kaiser et al. 2002), the Large Synoptic Survey Telescope (LSST; Tyson 2002), and the *Supernova Acceleration Probe* (*SNAP*; Aldering et al. 2002).

This work was supported in part with a scientific research grant (15204012) from the Ministry of Education, Science, Culture, and Sports of Japan (MEXT). M. A. is supported by a Grant-in-Aid for Young Scientists (B) from JSPS (18740118). This work is also supported in part with a scientific research grant (18072003) from the MEXT. We appreciate useful comments by Kimiaki Kawara and Željko Ivezić. We are grateful to all members of the SXDF project. We also thank the anonymous referee for useful suggestions, which improve the manuscript.

REFERENCES

Alard, C. 2000, A&AS, 144, 363
Alard, C., & Lupton, R. H. 1998, ApJ, 503, 325
Aldering, G., et al. 2002, Proc. SPIE, 4835, 146
Astier, P., et al. 2006, A&A, 447, 31
Barris, B. J., & Tonry, J. L. 2006, ApJ, 637, 427
Becker, A. C., et al. 2004, ApJ, 611, 418
Bertin, E., & Arnouts, S. 1996, A&AS, 117, 393
Boyle, B. J., Shanks, T., Croom, S. M., Smith, R. J., Miller, L., Loaring, N., & Heymans, C. 2000, MNRAS, 317, 1014
Brandt, W. N., & Hasinger, G. 2005, ARA&A, 43, 827
Brandt, W. N., Hornschemeier, A. E., Schneider, D. P., Alexander, D. M., Bauer, F. E., Garmire, G. P., & Vignali, C. 2001, ApJ, 558, L5
Chen, B., et al. 2001, ApJ, 553, 184
Cohen, S. H., et al. 2006, ApJ, 639, 731
Croom, S. M., Smith, R. J., Boyle, B. J., Shanks, T., Miller, L., Outram, P. J., & Loaring, N. S. 2004, MNRAS, 349, 1397
Dahlen, T., Strolger, L-G., Riess, A. G., Mobasher, B., Chary, R-R., Conselice, C. J., Ferguson, H. C., Fruchter, A. S., Giavalisco, M., Livio, M., Madau, P., Panagia, N., & Tonry, J. L. 2004, ApJ, 613, 189
de Vries, W. H., Becker, R. H., & White, R. L. 2003, AJ, 126, 1217
de Vries, W. H., Becker, R. H., White, R. L., & Loomis, C. 2005, AJ, 129, 615
Doi, M., et al. 2003, IAU Circ., 8119, 1
Eisenhardt, P. R., et al. 2004, ApJS, 154, 48
Fan, X., et al. 2006a, AJ, 131, 1203
———. 2006b, AJ, 132, 117
Fazio, G. G., et al. 2004, ApJS, 154, 10
Furusawa, H., et al. 2008, ApJS, in press (arXiv:0801.4017)
Giveon, U., Maoz, D., Kaspi, S., Netzer, H., & Smith, P. S. 1999, MNRAS, 306, 637
Groot, P. J., et al. 2003, MNRAS, 339, 427
Hatziminaoglou, E., et al. 2005, AJ, 129, 1198
Hawkins, M. R. S. 1996, MNRAS, 278, 787
———. 2002, MNRAS, 329, 76
Hawkins, M. R. S., & Veron, P. 1993, MNRAS, 260, 202
Hook, I. M., Jørgensen, I., Allington-Smith, J. R., Davies, R. L., Metcalfe, N., Murowinski, R. G., & Crampton, D. 2004, PASP, 116, 425
Hook, I. M., McMahon, R. G., Boyle, B. J., & Irwin, M. J. 1994, MNRAS, 268, 305
Huber, M. E., Everett, M. E., & Howell, S. B. 2006, AJ, 132, 633
Hughes, P. A., Aller, H. D., & Aller, M. F. 1992, ApJ, 396, 469
Ivezić, Ž., Vivas, A. K., Lupton, R. H., & Zinn, R. 2005, AJ, 129, 1096
Ivezić, Ž., et al. 2000, AJ, 120, 963
———. 2003, preprint (astro-ph/0310566)
———. 2004a, in ASP Conf. Ser. 327, Satellites and Tidal Streams, ed. F. Prada, D. Martinez Delgado, & T. J. Mahoney (San Francisco: ASP), 104
———. 2004b, in The Interplay Among Black Holes, Stars and ISM in Galactic Nuclei, ed. T. Storchi Bergmann, L. C. Ho, & H. R. Schmitt (Cambridge: Cambridge Univ. Press), 525
Iye, M., Ota, K., Kashikawa, N., Furusawa, H., Hashimoto, Tetsuya, Hattori, T., Matsuda, Y., Morokuma, T., Ouchi, M., & Shimasaku, K. 2006, Nature, 443, 186
Jha, S., et al. 2006, AJ, 131, 527
Kaiser, N., et al. 2002, Proc. SPIE, 4836, 154
Kashikawa, N., et al. 2002, PASJ, 54, 819
———. 2004, PASJ, 56, 1011
Kawaguchi, T., Mineshige, S., Umemura, M., & Turner, E. L. 1998, ApJ, 504, 671
Kodama, T., et al. 2004, MNRAS, 350, 1005
Koen, C., Kilkenny, D., van Wyk, F., Cooper, D., & Marang, F. 2002, MNRAS, 334, 20
Le Fevre, O., et al. 2003, Proc. SPIE, 4841, 1670
Lidman, C., et al. 2005, A&A, 430, 843
Liu, T., & Janes, K. A. 1990, ApJ, 360, 561
Lonsdale, C. J., et al. 2003, PASP, 115, 897
———. 2004, ApJS, 154, 54
Miyazaki, S., et al. 2002, PASJ, 54, 833
Morales-Rueda, L., Groot, P. J., Augusteijn, T., Nelemans, G., Vreeswijk, P. M., & van den Besselaar, E. J. M. 2006, MNRAS, 371, 1681
Ota, K., et al. 2007, ApJ, submitted (arXiv:0707.1561)
Ouchi, M., et al. 2004, ApJ, 611, 660
———. 2005a, ApJ, 620, L1
———. 2005b, ApJ, 635, L117
Pain, R., et al. 2002, ApJ, 577, 120
Perlmutter, S., et al. 1998, Nature, 391, 51
Phillips, M. M. 1993, ApJ, 413, L105
Poznanski, D., et al. 2007, 2007, MNRAS, 382, 1169
Rau, A., Greiner, J., & Schwarz, R. 2006, A&A, 449, 79
Rees, M. J. 1984, ARA&A, 22, 471
Richards, G. T., et al. 2006, ApJS, 166, 470
Richmond, M. 2005, PASJ, 57, 969
Riess, A. G., et al. 1998, AJ, 116, 1009
Robin, A. C., Reylé, C., Derrière, S., & Picaud, S. 2003, A&A, 409, 523
Rowan-Robinson, M., et al. 2005, AJ, 129, 1183
Saha, A., Thim, F., Tammann, G. A., Reindl, B., & Sandage, A. 2006, ApJS, 165, 108
Sako, M., et al. 2008, AJ, 135, 348
Sandage, A., & Tammann, A. G. 2006, ARA&A, 44, 93
Sarajedini, V. L., Gilliland, R. L., & Kasm, C. 2003, ApJ, 599, 173
Sarajedini, V. L., Gilliland, R. L., & Phillips, M. M. 2000, AJ, 120, 2825
Sarajedini, V. L., et al. 2006, ApJS, 166, 69
Schlegel, D. J., Finkbeiner, D. P., & Davis, M. 1998, ApJ, 500, 525
Schmidt, M. 1963, Nature, 197, 1040
Schneider, D. P., et al. 2005, AJ, 130, 367
Sekiguchi, K., et al. 2004, BAAS, 205, 8105
Sesar, B., et al. 2006, AJ, 131, 2801
———. 2007, AJ, 134, 2236
Sheinis, A. I., Bolte, M., Epps, H. W., Kibrick, R. I., Miller, J. S., Radovan, M. V., Bigelow, B. C., & Sutin, B. M. 2002, PASP, 114, 851
Simpson, C., et al. 2006, MNRAS, 373, L21
Smith, H. J., & Hoffleit, D. 1963, Nature, 198, 650
Strolger, L.-G., et al. 2004, ApJ, 613, 200
Sullivan, M., et al. 2006, ApJ, 648, 868
Terlevich, R., Tenorio-Tagle, G., Franco, J., & Melnick, J. 1992, MNRAS, 255, 713
Tonry, J. L., Howell, S. B., Everett, M. E., Rodney, S. A., Willman, M., & VanOutryve, C. 2005, PASP, 117, 281
Totani, T., Sumi, T., Kosugi, G., Yasuda, N., Doi, M., & Oda, T. 2005, ApJ, 621, L9
Tyson, J. A. 2002, Proc. SPIE, 4836, 10
Ueda, Y., et al. 2008, ApJS, submitted
Vanden Berk, D. E., Wilhite, B. C., Kron, R. G., Anderson, S. F., Brunner, R. J., Hall, P. B., Ivezić, Ž., Richards, G. T., Schneider, D. P., York, D. G., Brinkmann, J. V., Lamb, D. Q., Nichol, R. C., & Schlegel, D. J. 2004, ApJ, 601, 692
Vivas, A. K., & Zinn, R. 2006, AJ, 132, 714
Vivas, A. K., et al. 2004, AJ, 127, 1158
Watson, M. G., Roberts, T. P., Akiyama, M., & Ueda, Y. 2005, A&A, 437, 899
Yagi, M., Kashikawa, N., Sekiguchi, M., Doi, M., Yasuda, N., Shimasaku, K., & Okamura, S. 2002, AJ, 123, 66
Yamada, T., Kodama, T., Akiyama, M., Furusawa, H., Iwata, I., Kajisawa, M., Iye, M., Ouchi, M., Sekiguchi, K., Shimasaku, K., Simpson, C., Tanaka, I., & Yoshida, M. 2005, ApJ, 634, 861
Yasuda, N., et al. 2003, BAAS, 203, 8211
York, D. G., et al. 2000, AJ, 120, 1579